

Predicting aging-related decline in physical performance with sparse electrophysiological source imaging.

Vega-Hernández, Mayrim^{1,2}, Galán-García, Lídice², Pérez-Hidalgo-Gato, Jhoanna², Ontivero-Ortega, Marlis², García-Reyes, Ronaldo², Bosch-Bayard, Jorge³, Martínez-Montes, Eduardo^{2,*}, Marinazzo, Daniele⁴ and Valdés-Sosa, Pedro A.^{1,2,*}

¹The Clinical Hospital of Chengdu Brain Science Institute, MOE Key Lab for Neuroinformatics, University of Electronic Science and Technology of China, Chengdu, China.

²Cuban Center for Neurosciences, Havana, Cuba.

³Montreal Neurological Institute, Canada.

⁴Faculty of Psychology and Educational Sciences, Department of Data Analysis, Ghent University.

* Corresponding author at:

Cuban Center for Neurosciences, Human Brain Mapping Division, Havana, Cuba.

The Clinical Hospital of Chengdu Brain Science Institute, MOE Key Lab for Neuroinformatics, University of Electronic Science and Technology of China, Chengdu, China.

E-mail address: eduardo@cneuro.edu.cu; pedro.valdes@neuroinformatics-collaboratory.org.

This work was supported by the VLIR-UOS project “A Cuban National School of Neurotechnology for Cognitive Aging” and the National Fund for Science and Innovation of Cuba. CU2017TEA436A103. Partial funding was also provided by the Cuban National Program for Neuroscience and Neurotechnology, Project “Development of disease progression models for brain dysfunctions” PN305LH013-015.

HIGHLIGHTS

- Activation and connectivity from sparse/smooth/nonnegative ESI estimators of EEG theta rhythm are studied in elder subjects.
- ESI features revealed specific activation and connectivity patterns as predictors of aging-related gait-speed slowing.
- Stable features involved frontal and temporal areas previously reported as related to a higher risk of cognitive impairment.

ABSTRACT

Objective: We introduce a methodology for selecting biomarkers from activation and connectivity derived from Electrophysiological Source Imaging (ESI). Specifically, we pursue the selection of stable biomarkers associated with cognitive decline based on source activation and connectivity patterns of resting-state EEG theta rhythm, used as predictors of physical performance decline in aging individuals measured by a Gait Speed (GS) slowing.

Methods: Our two-step methodology involves estimating ESI using flexible sparse-smooth-nonnegative models, from which activation ESI (aESI) and connectivity ESI (cESI) features are derived. The Stable Sparse Classifier method then selects potential biomarkers related to GS changes.

Results and Conclusions: Our predictive models using aESI outperform traditional methods such as the LORETA family. The models combining aESI and cESI features provide the best prediction of GS changes. Potential biomarkers from activation/connectivity patterns involve orbitofrontal and temporal cortical regions.

Significance: The proposed methodology contributes to the understanding of activation and connectivity of GS-related ESI and provides features that are potential biomarkers of GS slowing. Given the known relationship between GS decline and cognitive impairment, this preliminary work opens novel paths to predict the progression of healthy and pathological aging and might allow an ESI-based evaluation of rehabilitation programs.

INDEX TERMS Electrophysiological source imaging, connectivity, gait speed, healthy aging, Stable Sparse Classifiers, multiple penalized-least-squares.

1. Introduction

The increase in life expectancy and the decline in the birth rate in recent decades have led to an aging population worldwide. The steady increase in the number of elder people

is accompanied by an increase in age-related diseases and disabilities. A key feature of aging is functional decline, which has far-reaching consequences for individuals, families, caregivers, and society. According to the WHO, around 55 million people worldwide live with dementia, with over 60%

of them in low- and middle-income countries. This number is expected to rise to 78 million in 2030 and to 139 million by 2050. In 2019, informal caregivers (mostly family and friends) spent around 5 hours on average daily, to provide care to people living with dementia. This produces a significant physical, emotional, and financial stress for the families and caregivers, with a huge economic impact (<https://www.who.int/news-room/factsheets/detail/dementia>). In this sense, brain function loss is one of the topics in the focus of current research on healthy aging. Although chronological age is strongly associated with age-related functional decline, there are substantial differences between individuals of the same age. Current neuropsychological evaluation is also highly subjective, leading to a large variability across subjects and strongly depending on the expertise of the evaluator.

Assessing individual changes in more direct measures of specific functional deficits could lead to objective ways to establish personalized biomarkers and early diagnosis of pathological aging. In this context, longitudinal studies are an ideal alternative to estimate the evolution of these deficits in an individual base, in conjunction with the selection of a biomarker system that explains the intrinsic mechanics of pathological aging. However, longitudinal assessment is not practical for a fast evaluation of cognitive decline. In this study we follow the approach of searching for objective measurements that can predict longitudinal changes and lead to determine possible biomarkers of aging-related decline taking into account individual changes.

The neural mechanisms of aging have been extensively studied using the electroencephalography (EEG), a portable, non-invasive and affordable technique that has become an appealing objective measurement for biomarker studies. Studies suggest that EEG can be a useful tool for assessing functional decline and cognitive changes associated with aging and different pathologies. An extensive literature reports a relationship between quantitative EEG (e.g. power spectrum) changes across different frequency bands and cognitive impairment (Pritchep et al., 2005). Musaeusa et al. (2018) found that increased theta power on the EEG is an early marker of cognitive decline in dementia due to Alzheimer's disease.

The high temporal resolution of EEG measurements has also led to studies exploring the use of functional connectivity measures among EEG electrodes to assess changes that occur with aging. There is evidence to consider that the ensemble of information between functionally specialized regions defines a functional brain connectivity that is fundamentally essential for cognition (Bressler & Menon, 2010). Some authors believe that this connectivity can be reflected in electroencephalography (EEG) (Horwitz, 2003) but the influence of volume conduction effects makes it very unlikely (Paz-Linares et al., 2023) since the EEG only gives widespread spatial maps that do not directly reflect those regions involved in brain functional networks. In any case, the use of both quantitative EEG and functional EEG connectivity as a biomarker of cognitive impairment is still

an active area of research ((Smailovic et al., 2018) and for review see (Smailovic & Jelic, 2019)).

Although less explored, estimating the EEG source activation and connectivity with Electrophysiological Source Imaging (ESI) is known to provide relevant information about the functional organization of the brain and interregional communication (Paz-linares et al., 2023; He et al., 2019; Van de Steen et al., 2019). EEG source images have also been used to investigate changes in brain function associated with both healthy aging and neurodegenerative diseases, including Alzheimer's disease and Parkinson's disease (Jabès et al., 2021; Meghdadi et al., 2021; Muthuraman et al., 2014). Babiloni et al. (2018) investigated the functional connectivity of alpha rhythm sources in MCI patients, while Vecchio and colleagues evaluated the risk of MCI progression using EEG connectivity and graph theory combined with Apolipoprotein E (Vecchio et al., 2018). Hata and colleagues established that cerebrospinal fluid biomarkers of Alzheimer's Disease correlated with EEG source parameters (mean activation and lagged phase synchronization) as assessed by exact low-resolution electromagnetic tomography (eLORETA) (Hata et al., 2017).

In most of these studies, source activation and connectivity analyses were performed from the EEG sources estimated using the LORETA (or its version sLORETA, eLORETA) (Pascual-Marqui et al., 1994; Pascual-Marqui, 2002; Pascual-Marqui, 2007) inverse solver, a well-known methods that produces images with low spatial resolution inside the brain (Babiloni et al., 2018; Vecchio et al., 2018; Hata et al., 2017).

However, one approach that has gained attention in recent years is the estimation of sparse ESI which produces source images with higher spatial resolution by aiming at minimizing the number of active sources and maximizing their contributions to the observed EEG signals (Knösche & Haueisen, 2022). In addition, the development of efficient algorithms such as the Active-set Modified Newton Raphson (AMNR) to address flexible Multiple Penalized Least Squares (MPLS) models allows to find ESI solutions that combine different degree of smoothness and sparseness, and can also include sign constraints (Vega-Hernández et al., 2019)

It is also noticeable that current studies have mostly attempted to extract biomarkers by analyzing activation and connectivity separately, leading to reports of two different and seemingly unrelated patterns. Obviously, the high dimensionality of the analysis becomes more critical when considering both patterns at once. The combination of a suitable variable selection method and dimensionality reduction techniques would be necessary to address the problem of combining both activations and connectivity information to find a unique pattern. Many methods of variable selection have been developed for high-dimensional data. However, model stability (i.e., the robustness of the selected model against small perturbations of the data set) is essential and cannot always be ensured or even assessed. The combination of resampling techniques to evaluate the stability of the models when performing penalized regressions opens

the way to obtain stable estimation of the biomarkers (Bosch-Bayard et al., 2018). This would be crucial for ensuring the validity and reliability of the results obtained from the generally ill-conditioned penalized regression.

In this paper we introduce a methodology that combines two main steps: 1) the estimation of features from the EEG based on the sparse activation and connectivity ESI as a multivariate system, and 2) the identification of stable sparse biomarkers from these ESI features that predicts changes in specific measures of functional decline.

Although the methodology is general in the sense that it can be applied using any ESI model and feature, as well as predicting any functional change, in this work we will use the patterns of activation and connectivity ESI from the EEG theta rhythm, in order to find a “biomarker system” for cognitive decline. Specifically, we will use data from a longitudinal study in healthy elder adults, where the walking or gait speed (GS) was measured in two different appointments separated by an interval of 6 years. In the last assessment, resting-state EEG was acquired in all participants. GS has been used in the clinical practice as a predictor of adverse outcomes (Kahya et al., 2019; Afilalo et al., 2016) and an important biomarker of human health (Nascimento et al., 2022; Skillback et al., 2021), which has even been described as the “sixth vital sign” (Fritz and Lusardi, 2009). GS is also one of the most attractive physical biomarkers of cognitive decline (Nascimento et al., 2022; Cohen and Verghese, 2019; Kahya et al., 2019). Some studies using GS and cognitive tasks have found consistent results on poor performance in various independent gait domains preceding cognitive decline and incident dementia (e.g., Skillback et al., 2021; Darweesh et al., 2019; Dumurgier et al., 2017).

Therefore, with the methodology introduced in this work, we aim at preliminarily exploring the capability of a transversal EEG measurement to predict longitudinal changes in the GS on individual basis. This may contribute to a better understanding of the neural bases of gait changes that may reflect some cognitive impairment, as well as propose novel paths to predict the progression of healthy and pathological aging and might even provide tools for an ESI-based evaluation of rehabilitation programs.

2. Materials and methods

2.1 General methodology

With the aim to investigate the ability of activation and/or connectivity ESI to predict cognitive decline in aging subjects we propose the methodology whose scheme is illustrated in Figure 1. In short, there is a first block of data acquisition and pre-processing that allows the researcher to start from a clean piece of EEG data and decide if ESI features are going to be derived from time or frequency domain, or even after using more sophisticated processing of the EEG such as PCA, ICA, time-frequency or multidimensional analysis. The block for Step 1 represents the computation of specific inverse methods and ESI features, as well as the definition of nodes for the

connectivity analysis and the standardization of the final features. The block for Step 2 includes the use of classifiers or any other method for biomarker -variable- selection from the features obtained from Step 1. The following subsections will explain the details of each block for the presented study.

2.2 Data acquisition and pre-processing

2.2.1 Subjects

The dataset used in this study is composed of EEG signals recorded from 66 community-dwelling adults who regularly practiced mild-to-moderate exercise in their communities (García-Agustin et al., 2020). The age range of the participants varies from 64 to 94 years old (mean age: $78,73 \pm 6,69$ years). These subjects were a subsample from a longitudinal study conducted in Havana from 2007 to 2016. For this study we selected the subsample of subjects that were clinically evaluated in 2010 and 2016, specifically with measurements of physical performance, such as the gait speed (GS). In 2016, the subjects were reassessed and a resting-state EEG was additionally acquired in all participants.

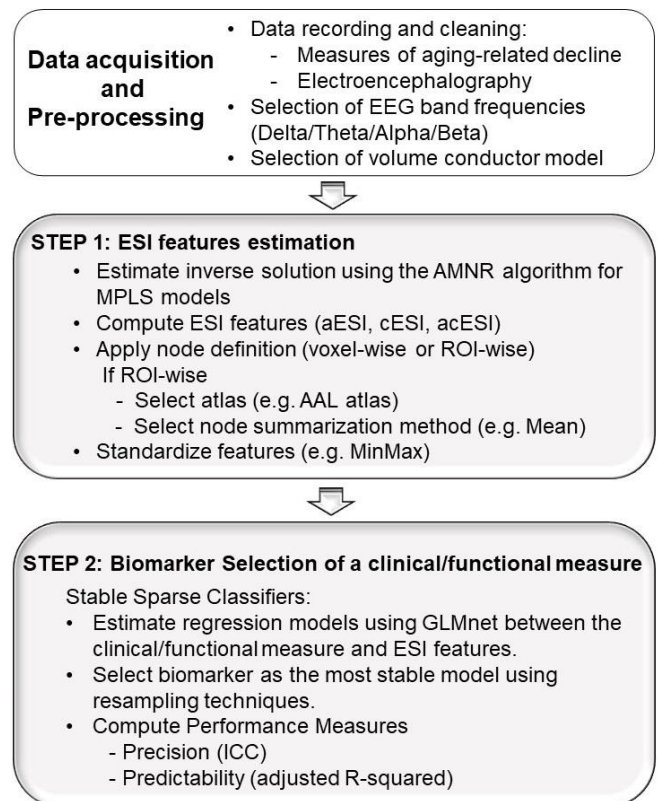


Fig. 1. Schematic representation of the proposed methodology to use features derived from Electrophysiological Source Imaging as predictors of changes in a clinical/functional measure of cognitive decline (in our case changes in gait speed).

2.2.2 Recording of Gait Speed

The 4-Meter Walk Test (4MWT) quantified the GS with high test-retest reliability and validity (Peters et al., 2013). This technique requires a stopwatch and a facility hallway and

can be performed by non-professional trained staff (Tzemah-Shahar et al., 2022; Fritz & Lusardi, 2009). The measurement consisted in quantifying the time spent to cover 4 meters at a normal pace and was expressed in meters per second (m/s). Individual gait speed variability (Delta Gait Speed, DGS) was calculated for each subject as the difference between the two measured gait speeds (in 2010 and 2016), relative to the initial GS.

2.2.3 EEG recordings

The EEG data were recorded using the Neuronics EEG recording system MEDICID 5-32 system. Nineteen Ag/AgCl electrodes were placed on the scalp according to the international 10/20 electrode placement system, taking the linked earlobes as the reference and keeping electrode impedance below 10 kOhm. The EEG was acquired at rest for 10 minutes, while the participants were asked to close and open their eyes at different times to explore reactivity and avoid drowsiness.

The sampling period was 5 ms. Epoch selection during the eyes-closed resting-state was carried out offline using Neuronics EEG analysis (Neuronics SA), obtaining 18 to 24 artifact-free segments of 2.56 s for each subject by visual inspection of two experienced neurophysiologists. The Fast Fourier Transform (FFT) was applied to those artifact-free EEG epochs to find the complex EEG values in the frequency domain, which were averaged in the theta band. The spectra was calculated from 0.39 to 19.14 Hz yielding a parameter matrix of 49 frequencies for each of the 19 recorded electrodes, where the Theta band was defined from 5.47 to 7.03 Hz (Babiloni et al., 2020; Bosch-Bayard et al., 2001).

A standard template head model was used for estimating ESI on all subjects. The generating sources were defined over a mesh of the cortical surface containing 5656 vertices on brain regions that are physiologically feasible EEG generators (e.g., avoiding vertices in corpus callosum). Using a three-sphere piece-wise homogenous and isotropic head model, the design matrix (known as the Electric Lead Field) was computed for the standard positions of the array of 19 electrodes from the 10/20 system in Neuronics Source Localizer (Riera & Fuentes, 1998).

2.3 STEP 1: Estimation of ESI features

Electrophysiological Source Imaging (ESI) consists in the estimation of the brain source activity (reflected by the macroscopic primary current density produced by synchronized post-synaptic potentials of masses of spatially coherent pyramidal neurons) from the scalp potentials measured with the EEG. This is mathematically an ill-posed problem due to the non-uniqueness of the solution, thus finding a solution requires using additional or prior information about the properties of the EEG sources. A large family of distributed source reconstruction methods, also called minimum norm methods, has been developed (Knösche & Haueisen, 2022) based on MPLS models. A well-known member of this family is the Low Resolution

Electromagnetic Tomography (LORETA) (Pascual-Marqui et al., 1994), which includes only an ℓ_2 -norm penalty to enforce a smooth solution. The use of ℓ_1 -norm penalties has also been tested to force solutions to be sparse and/or piecewise sparse e.g., the Least Absolute Shrinkage and Selection Operator, LASSO (Tibshirani, 1996) and its variants (Kim et al., 2018). However, the lack of a ground truth has encouraged using more flexible models that allow finding solutions with different degrees of sparsity and smoothness (Vega-Hernández et al., 2008, 2019; Haufe et al., 2008, 2011; Sohrabpour et al., 2016). A general theoretical framework for doing this is provided by the Multiple Penalized Least Squares (MPLS) model, which allows a common formulation of a large variety of solutions. However, using efficient algorithms to estimate these flexible MPLS models is critical to address real-world EEG data's complexities effectively. Recently, we proposed the Active-Set Modified Newton-Raphson (AMNR) algorithm that extends the LARS algorithm to find solutions along the Newton-Raphson update direction (Vega-Hernández et al., 2019) (Matlab code available at <https://portal.cbrain.mcgill.ca/>). This algorithm allows efficient estimation of solutions combining smoothness and sparseness but also including sign constraints in a natural way (Vega-Hernández et al., 2019).

In this work, the ESI was estimated using the general MPLS model and the AMNR algorithm for three representative methods: the version of LORETA, which imposes smoothness, the Elastic Net L that imposes a combined smoothness/sparsity and the Non-Negative Smooth LASSO, which imposes non-negativity constraints to smooth/sparse solutions. The mathematical formulation of each method within the general MPLS framework is provided in Table 1. The estimated magnitude with each of these methods will be called the activation ESI (aESI) and will be a first ESI feature to be assessed as a potential biomarker. This can be obtained in both time and frequency domain (i.e., amplitude spectrum). A second ESI-derived feature would reflect the brain connectivity at the source level. This can be also obtained from time-domain correlation/autoregressive models or from frequency-domain measures assessing the statistical or causal relationship between source activity (e.g., Granger causality, Coherence, phase locking value, etc.) (He et al., 2019). In this study we use the source cross-spectra, estimated as the covariances of activation ESI in the Theta band along all segments of eyes-closed resting-state EEG (Marinazzo et al., 2019; Van DeSteen et al., 2019). The symmetric covariance matrix contains information of the level of activation (in the variances, in the diagonal elements) and of the connectivity (in the off-diagonal elements). We here use a vector of all pairwise covariances as the connectivity ESI (cESI) feature. A third feature allows to explore the combination of both information by forming a vector containing both variances and covariances, which will be called activation/connectivity ESI (acESI).

Two important factors need to be taken into account. On one hand, aESI (cESI) feature gives one value for each source generator (pairs of source generators), i.e., they provide vertex-wise or voxel-wise magnitudes. The voxel-wise activations and connectivity have in principle a high spatial resolution, but it is known that they will present a higher risk of reflecting spurious activations and short-range connectivity due to partial volume/smoothing effects, making it difficult to assess their validity. In addition, the processing of all individual activations and pairwise connections is computationally demanding. Therefore, we here opted to explore the voxel-wise feature only for aESI, while parallel for the three ESI features (aESI, cESI and acESI) we reduced the dimensionality by summarizing the features using regions of interest (ROIs) according to a specified anatomical atlas. This step might facilitate the interpretation of the selected

biomarkers in terms of brain regions and not just individual voxels. In particular, we use the Automated Anatomical Labeling (AAL) segmentation from the Montreal Neurological Institute atlas (Tzourio-Mazoyer et al., 2002) for computing the activation and connectivity in 76 anatomical compartments as the mean value across all sources (vertices of the cortical mesh) included in each ROI (see labels in Fig. S1 and Table S1 in the Supplemental Material) On the other hand, ESI-derived features will also reflect the large inter-subject variability typical of the EEG and ESI. Although there is no easy way to know if a normalization of the individual data is necessary for finding group effects, we decided to use a Mix-Max standardization of all features, both voxel-wise or ROI-wise, to get normalized values for each subject in the range [0,1] and facilitate the implicit comparison when selecting the potential biomarker models.

Table 1. General formulation of an MPLS model (top row). Next rows show the specific expression of the penalty term for the models: LORETA, ELASTIC Net (ENET L) and Nonnegative Smooth LASSO (NN-SLASSO). \mathbf{V} represents the EEG data matrix, \mathbf{J} is the unknown primary current density reflecting source activity, \mathbf{K} is the Electric Lead Field, \mathbf{L} is the matrix of second differences, or any other roughness operator, and λ_r represent the regularization parameters.

MPLS solutions: $\hat{\mathbf{J}} = \underset{\mathbf{J}}{\operatorname{argmin}}\{\ \mathbf{V} - \mathbf{KJ}\ _2^2 + \Psi(\mathbf{J})\}$ with $\Psi(\mathbf{J}) = \sum_{r=1}^R \lambda_r \sum_{i=1}^{N_r} \mathbf{g}^{(r)}(\theta_i^{(r)})$		
Penalty function: $\mathbf{g}^{(r)}: \mathbb{R} \mapsto \mathbb{R}$, are symmetric, non-negative, non-decreasing and continuous over $(0, +\infty)$		

Name	Penalty term $\Psi(\beta)$	Function definitions for all models
LORETA	$\lambda_1 \sum_{i=1}^p \mathbf{g}^{(1)}(\theta_i^{(1)})$	$\mathbf{g}^{(1)}(\theta) = \theta^2$; $\theta^{(1)} = \mathbf{LJ}$
ENET L	$\lambda_1 \sum_{i=1}^p \mathbf{g}^{(1)}(\theta_i^{(1)}) + \lambda_2 \sum_{i=1}^p \mathbf{g}^{(2)}(\theta_i^{(2)})$	$\mathbf{g}^{(2)}(\theta) = \theta $; $\theta^{(2)} = \mathbf{LJ}$
NN-SLASSO	$\lambda_1 \sum_{i=1}^p \mathbf{g}^{(1)}(\theta_i^{(1)}) + \lambda_2 \sum_{i=1}^p \mathbf{g}^{(3)}(\theta_i^{(3)})$	$\mathbf{g}^{(3)}(\theta) = \theta $; $\theta^{(3)} = \mathbf{J}$ subject to $\mathbf{J} \geq \mathbf{0}$

2.4 STEP 2: Biomarker selection

A general methodology to select potential biomarker models from a pair of dependent and independent variables was presented by Bosch-Bayard and colleagues in the Stable Sparse Classifiers (SSC) procedure (Bosch-Bayard et al., 2018) (code in <https://github.com/tperezdevelopment/biomarkers>). The procedure is based on the following steps:

- Use penalized regression as a variable selection method. In particular, the elastic-net model (Zou & Hastie, 2005) as implemented in the GLMnet package for Matlab (<http://www-stat.stanford.edu/~tibs/glmnet-matlab/>), which correspond to the optimization problem:

$$\hat{\beta} = \operatorname{argmin}\{\|\mathbf{Y} - \mathbf{X}\beta\|_2^2 + (1 - \gamma)\|\beta\|_2^2 + \gamma\|\beta\|_1\}$$

Here, $\mathbf{Y} \in \mathbb{R}^N$ is the dependent variable, in our case the measure of aging-related decline (delta gait speed) for each of

the N subjects; \mathbf{X} is the independent variable conforming a design matrix where each row represents the vector ESI-derived feature for each subject; $\beta \in \mathbb{R}^p$ are the model parameters or regression coefficients for each of the p elements of the ESI feature; γ is the regularization parameter; and $\|\cdot\|_1$ and $\|\cdot\|_2$ represent the ℓ_1 -norm and ℓ_2 -norm, respectively.

- Use quantitative indicators to assess the stability of the selected variables (significant regression coefficients). Subsampling the data in both dimensions, the observations and the variables, make it possible to obtain a number of subsamples to estimate the regression coefficients in each one. Variables that are selected on a large fraction of the subsampled data after several iterations are considered significantly stable features. The principle is that if some features are consistently significant across all models, they can point to variables that are strong indicators of a potential stable biomarker. We will report the replicability of a variable as measured by the percentage of times that the variable is included in the selected models.

- The evaluation of the performance of the classifier using performance measures. The method calculates the receiver operator characteristic (ROC) and area under the curve for each model in each input subsampled data. This allows estimating the probabilistic distribution of the area under the ROC curve and therefore provides the possibility of combining the criteria of stability and precision for the selection of the model with statistically higher performance.

In addition, this methodology provides performance measures such as the adjusted R-square (R2) and intraclass correlation coefficient (ICC) for the highest performing selected model. The first gives a general measure of goodness of fit and predictability. The ICC can be interpreted as a generalized measure of the precision of the model. The ICC estimator is:

$$ICC = (MS_R - MS_W) / (MS_R + (k - 1)MS_W)$$

were MS_R = mean squares of model; MS_W = mean squares for residual sources of variance; k = number of measurements (Koo & Li, 2016).

There are no standard values for acceptable reliability using ICC but previous studies suggest that ICC values less than 0.5 indicate poor reliability, values between 0.5 and 0.75 indicate moderate reliability, values between 0.75 and 0.9 indicate good reliability, and values higher than 0.90 indicate excellent reliability (Koo & Li, 2016; Liljequist et al., 2019).

3. RESULTS

3.1 Data characterization

The statistical behavior of the longitudinal changes in the measured gait speed, i.e., the delta gait speed (DGS), as well as of the initial and final GS (measured in 2010 and 2016, respectively) are shown in Table 2. The initial and final GS values are significantly different in the group of subjects (T-test for dependent samples: $t(65) = 10.36, p < 0.01$).

Table 2. Descriptive statistics for gait speed (GS) variables.

SD = standard deviation, CI = confidence interval (95%)

Variable	Mean (\pm SD)	CI
GS initial	1.036 (\pm 0.28)	[0.968, 1.103]
GS final	0.753 (\pm 0.21)	[0.701, 0.804]
DGS	-0.254 (\pm 0.20)	[-0.303, -0.204]

3.2 Relationship between aESI and gait speed changes.

We first made an exploratory analysis of the relationship between ESI-derived features and the changes in gait speed. Correlation maps between aESI and DGS along all subjects were computed for each method (LORETA, ENETL and NN-SLASSO). Statistically significant correlations were assessed by a permutation test (50000 permutations) that corrected for multiple comparisons by using the empirical distribution of the maximum t-value. This analysis was performed at the two

different spatial levels, i.e., using voxel-wise and ROI-wise aESI.

Figure 2, panel A, illustrates the correlation map for the 3 aESI estimation methods. (The scale corresponds to the percentile of the probability observed under the null hypothesis of no correlation in each voxel $p < 0.05$). The LORETA method did not show significant correlations. The ENET-L and NN-SLASSO methods show significant differences in the inferior and middle left temporal, left frontal, and occipital regions. A plausible explanation for this result may be the spatial smoothness that the Loreta method yields with respect to the others.

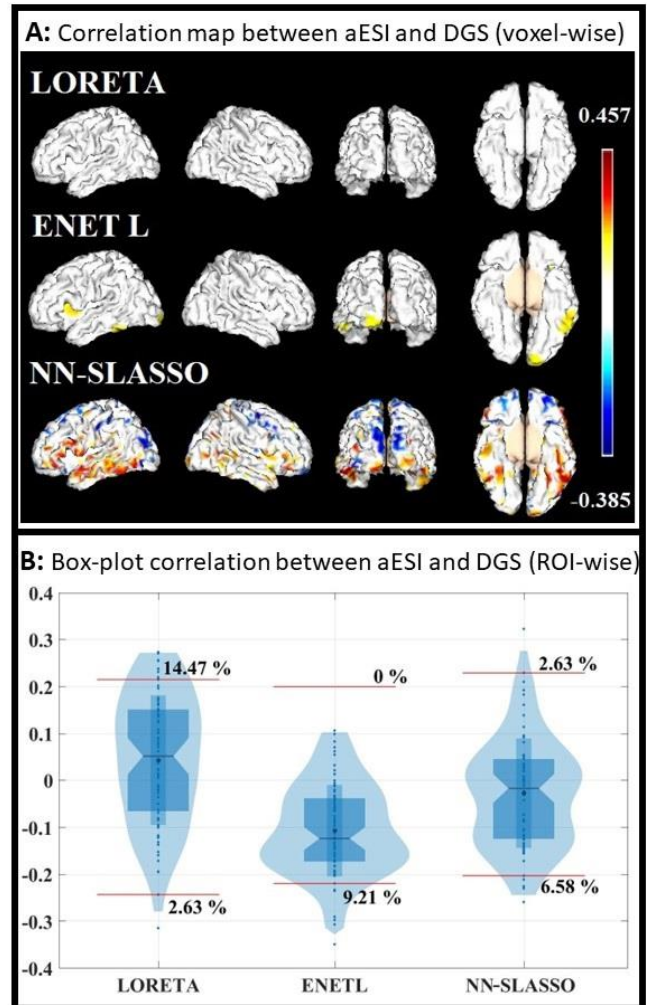


Fig. 2. Panel A: Four views (left, right, back and bottom) images of the significant correlation map between voxel-wise aESI and Delta Gait Speed (DGS). Correction for multiple comparisons was performed with 50000 permutations. The color bar represents the correlation value. Panel B: Box-plot of the correlation between aESI and DGS in ROI-wise. In each tail, we show the significance threshold and the percentage of ROIs whose aESI was significantly correlated with DGS.

Figure 2, panel B, shows the distribution of correlation values between ROI-wise aESI and the DGS. In each box-plot, the horizontal bar denotes the threshold in both tails (horizontal red lines) and the percentage of the total number of ROIs that yielded significant values are shown. LORETA

led to the greatest number of significant ROIs among the three aESI, contrary to the result of no significant voxels found in the voxel-wise correlation analysis. This could be explained by the low resolution of LORETA ESI which could lead to a significant level in the ROI analysis along subjects despite low variability in the voxel level. For the ENET L and NN-LASSO methods, there was agreement between the two correlation analyses. In the case of ENET L we found seven ROIs with significant negative correlation, with the parahippocampal, fusiform, and temporal middle right regions presenting the highest absolute values. For the NN-SLASSO we localized seven ROIs with significant positive and negative correlation, where the inferior temporal bilateral (+) and superior frontal orbital right (-) regions showed the highest absolute values. Table S2 of the Supplemental Material summarizes the location of the significant regions for each method.

3.3 Biomarkers selection from ESI-derived features

We here explore the performance as potential biomarkers of nine adjusted model features corresponding to the three MPLS methods (LORETA/ENET L/NN-SLASSO) and the three ESI-derived features (aESI/cESI/acESI). Figure 3 represents graphically the mean intraclass correlation coefficient (ICC) and its confidence interval (ICC-CI) in each case. In addition, the p-value associated with the ICC, the adjusted R^2 and its p-value provided by the SSC are shown in Table 3.

For all methods, the ICC value was preserved or increased when taking into account connectivity features as compared to the use of activation only. In addition to estimation of ICC, a hypothesis test is performed with the null hypothesis that $ICC = 0$. The F value, degrees of freedom and the corresponding p-value of this test are reported in Table 3. Although all methods and features showed ICC and R^2 significantly different from zero (F-test), ENET L showed the lowest values for all features and those that changed the least with the inclusion of connectivity. LORETA presented low prediction with mean ICC values below 0.5, although the values increased significantly for ROI-wise cESI and acESI with respect to aESI (F-test, $p\text{-value} \ll 0.01$, Table 3). The acESI feature estimated by the NN-SLASSO presented the best performance of all cases: the highest mean and smallest variances with a significant increased when using cESI and acESI with respect to aESI (F-test, $p\text{-value} \ll 0.01$). The acESI from NN-SLASSO may be considered a moderate/suitable predictor of the changes in GS (as reflected by the moderate predictive power $0.50 < ICC < 0.75$ (Koo & Li, 2016; Liljequist et al., 2019). The adjusted R^2 showed the same behavior, although LORETA and ENET L presented similar values and significance, while NN-SLASSO showed better performance. Table S3 of the Supplemental Material shows more details on.

These results suggest that the patterns of activation and connectivity obtained from the NN-SLASSO model, that showed the best performance according to the ICC and the

stability index, can be considered as possible biomarkers associated with the change in gait speed.

Figure 4 shows these patterns in three panels. Panel A shows the activation pattern of the ROI-based aESI feature, scaled by the value of regression coefficients for each ROI included in the biomarker model. The main ROIs include the superior frontal orbital right, postcentral right and inferior temporal bilateral. The stability of the coefficients associated with each ROI is in the range of 41.2% and 58.4% (see Table S4 of the Supplemental Material)

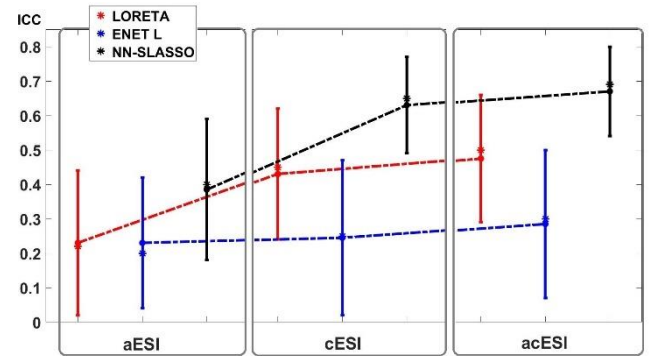


Fig. 3. The intraclass correlation coefficient (ICC) and its confidence interval from each feature (aESI, cESI, acESI) and model (LORETA in red, ENET L in blue and NN-SLASSO in black) to predict the variation of the gait speed.

Table 3. Performance of models as biomarkers for each feature and ESI model.

Feature	Methods Name	p-value of ICC	R^2	p-value of R^2
aESI	LORETA	0.0349	0.15	0.0021
	ENET L	0.0490	0.15	0.0032
	NN-SLASSO	0.0004	0.29	0.0000
cESI	LORETA	0.0001	0.33	0.0000
	ENET L	0.0184	0.26	0.0001
	NN-SLASSO	0.0000	0.59	0.0000
acESI	LORETA	0.0000	0.37	0.0000
	ENET L	0.0065	0.27	0.0001
	NN-SLASSO	0.0000	0.62	0.0000

Panel B shows 149 possible connectivity biomarkers from the cESI feature.

Panel C shows the activation map and the connectivity pattern associated with the acESI model. Biomarker patterns associated with activation only versus activation and connectivity are highly consistent, except in the right postcentral region in blue. For acESI model, 152 possible connectivity biomarkers are estimated. The connection between inferior temporal in both hemispheres, left frontal inferior triangular and right fusiform, presented the model's highest replicability (over 98th percentile). On the other hand, the connections between the left precuneus and cingulate middle and right posterior; left insula and left cuneus; showed the highest positive beta values (over the 98th percentile of the absolute value of betas) in the model. Also, a negative beta value was obtained for a connection from the right supp-motor area and the right hippocampus.

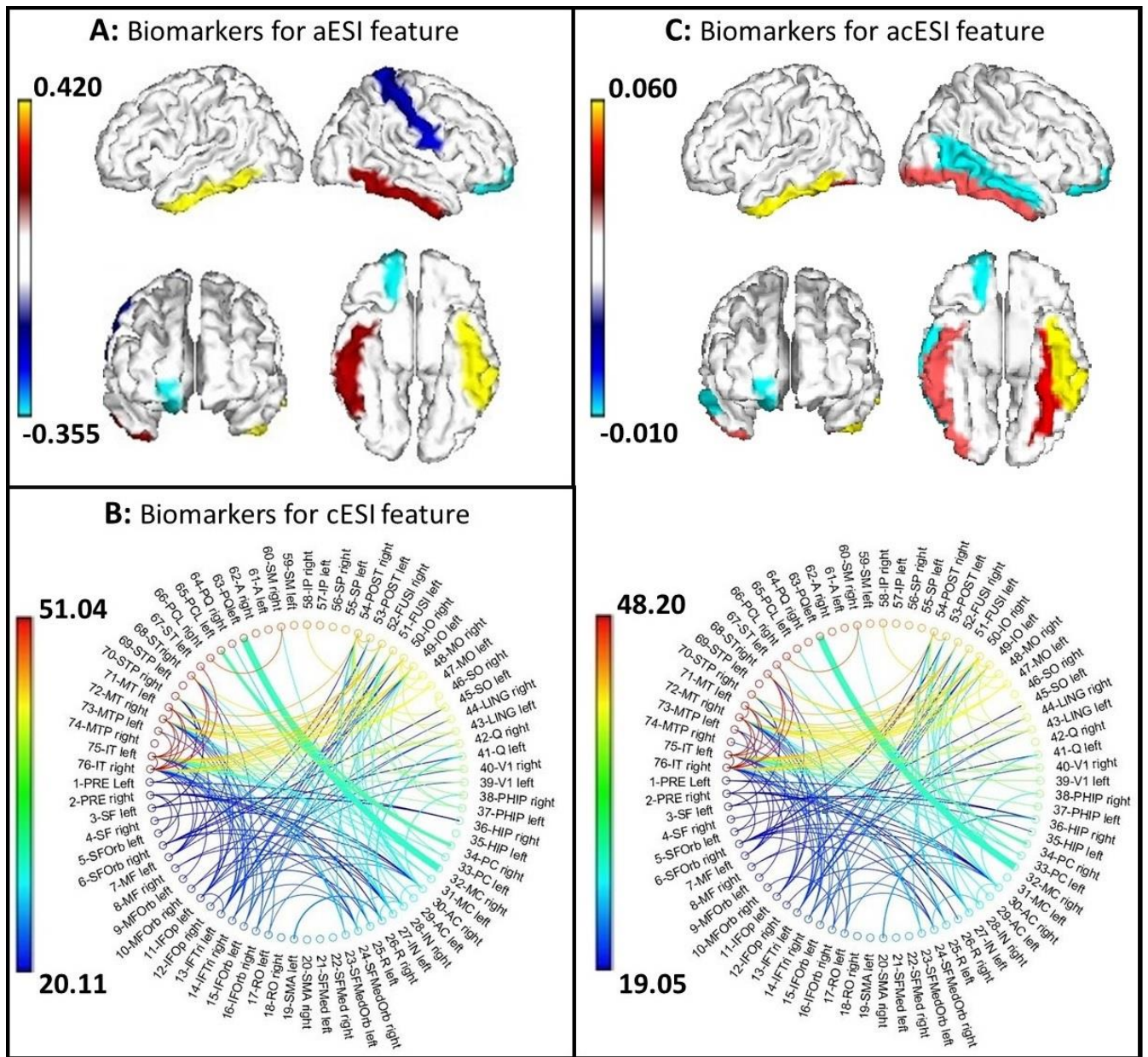


Fig. 4. Weights associated of candidate biomarker for gait speed change. **Panel A** shows a four-view (left, right, front, and bottom) activation Electrophysiological Source Imaging (aESI) where four ROIs are considered biomarkers and are highlighted in different colors (right front-orbital superior in cyan, right postcentral in blue, left and right inferior temporal in yellow and red; respectively). The color bar represents the value of estimated coefficients. **Panel B** shows a graph representation of the connectivity Electrophysiological Source Imaging (cESI) where the width of the connection represents the value of the beta coefficients of the estimated model. The color bar represents the replicability of each variable. **Panel C (Top)** shows the acESI biomarkers appearing in four views (left, right, front, and bottom). The elements considered biomarkers from the diagonal of the cross-spectra matrix, were found in fifes ROIs (right fronto-orbital superior, left and right inferior temporal, left fusiform and right middle temporal). The color bar represents the value of estimated coefficients. **Panel C (bottom)** shows a graph representation of the off-diagonal elements of the cross-spectra matrix. There, the width of the connection represents the value of the beta coefficients of the estimated model. The color bar represents the replicability of each variable. All variables selected in each model are reported in Tables S4 – S6 of the Supplemental Material

4. DISCUSSION

Resting-state EEG activation and connectivity patterns provide essential information about the functional organization of the brain and interregional communication. However, the selection of early biomarkers of cognitive impairment using joint patterns of activation and

connectivity of EEG sources has been poorly studied and faces validity and applicability challenges. Factors such as the experimental design, the measure chosen as the dependent variables, the spatial resolution of the set of nodes (e.g., region of interest (ROI) vs. single vertices (voxel)) and the methods of analysis, can influence the results and limit its validity and potential extension. The variability introduced by EEG recording systems and protocols also

affects the replicability of the results. In addition, among the challenges of determining biomarkers are the high dimensionality of ESI related features and the need for the selection of a robust prediction method.

Some of these challenges may be addressed with some known approaches but other deserve future thorough studies and creative strategies. For instance, the high variability of evaluation measures can be handled by considering experimental designs from longitudinal studies, which allows estimating the basal state inter-individually (Smailovic & Jelic, 2019). The low replicability due to the variability introduced by recording protocols, can be corrected by applying novel harmonization methods to the collected data (Jovicich et al., 2019; Li et al., 2022). The variability introduced due to the variable selection method can be controlled by using performance measures based on the stability of the estimated biomarkers.

The principal outcomes of this paper are to provide a methodology that is easily replicable, to contribute to a better understanding of the role of activation and connectivity ESI patterns as related to gait decline, and to provide features that can become potential biomarkers of cognitive decline. We applied the proposed methodology to a real data sample from a longitudinal study carried out over nine years in adult subjects (García-Agustin et al., 2020).

Why predicting changes in GS?

In our approach, we attempt to predict the individual changes in gait speed (GS) over a period of 6 years, in subjects that did not show advanced symptoms of cognitive impairment, from ESI-derived features obtained in only one moment (transversal measurement). GS has been shown to be an early proxy of the aging-related cognitive decline (Öhlin et al., 2020, 2021; Montero-odasso et al., 2020; Zhou et al., 2021; Skillbäck et al., 2021; Collyer et al., 2022; Nascimento et al., 2022). Some works have reported the study of the relation between GS and EEG (Nordin et al., 2020; Min et al., 2022; Sanctis et al., 2023) using generally the EEG spectrum. Other morphometric studies have used structural magnetic resonance imaging (MRI) to show that there is a relationship between gray matter volume and GS, mainly in frontal, occipital and hippocampal regions, as well as in basal ganglia and cerebellum (Voelcker-rehage et al., 2011; Wilson et al., 2019). Some of these regions are also found in our results. Additionally, research using EEG has found that the connectivity patterns between these regions may also be related to gait impairments in aging individuals (e.g., Huang et al., 2020). Previous longitudinal studies on GS and cognition have indicated that GS changes occur as early as 7 to 12 years before dementia development (Dumurgier et al., 2017). Skillbäck et al. (2021) demonstrated that accelerated GS decline preceded cognitive decline and indicated that faster GS decline is seen when conversion into detectable cognitive deficiency is imminent.

Why using activity and connectivity ESI as features?

In the search for potential biomarkers of the changes in GS, the independent variable (i.e., features) were the activity and/or connectivity ESI, estimated from three different MPLS models with different penalty combinations to compare the influence of the degree of smoothness/sparseness of estimated activation (Vega-Hernández et al., 2019). The selection of those features with the highest predictability and/or stability was carried out using the Stable Sparse Classifiers (SSC) procedure (Bosch-Bayard et al., 2018).

In particular, the average amplitude of the individual EEG frequency spectrum in the theta band was chosen for source estimation using ESI. Previous studies have already considered the theta band for the identification of biomarkers in the study of cognitive decline (Musaeus et al., 2018; Babiloni et al., 2016; Hata et al., 2016; Cozac et al., 2016). However, most of the studies searching for biomarkers in source activity/connectivity have only used very smooth ESI, such as those obtained with the LORETA family (LORETA, sLORETA, eLORETA) (Pascual-Marqui et al., 1994; Pascual-Marqui, 2002; Pascual-Marqui, 2007). There are few reports of studies using sparse ESI or other methods based on the MPLS methodology. In one of these works, Prichep and colleagues used EEG inverse solutions in frequency domain (VARETA) for the early detection of cognitive decline (Prichep, 2007). Prichep (2007) found similar results to our study, by showing that the EEG theta band predicts future cognitive decline or conversion to dementia with high accuracy, but they do not include connectivity analysis as a possible biomarker. In a previous preliminary study, we showed that using sparse and sparse/smooth/nonnegativity constraints in combination models for aESI estimation provides more flexibility and adaptability to find complex multisource patterns as those appearing in real data in normal and pathological aging (Vega-Hernández et al., 2022).

In this work, we used the same approach, taking advantage of the AMNR algorithm that allowed for a fast estimation of the different models (Vega-Hernández et al., 2019). We tested the Ridge L solution as a version of LORETA, the ENET L model that combines penalties that induce smoothness and sparsity simultaneously, and the NN-SLASSO, which also combines smoothness and sparsity but adding a nonnegative constraint to the activation. Although the negative values of the activation ESI obtained in a mesh of the cortex can be related to equivalent current dipoles pointing in the opposite direction, the nonnegativity constraint here reflects our prior belief that the most probable sources correspond to current dipoles that are similarly oriented (perpendicular to the cortex) with an origin in masses of pyramidal neurons. ESI obtained from these models has shown to have different sparsity and ability to estimate sources of EEG activity. However, the high inter-individual variability of the solution and the lack of a ground truth makes it impossible to have a final answer about which

is the best model to estimate ESI when applied to real EEG data (Vega-Hernández et al., 2022).

We have then tested and compared the predictive ability of activity and connectivity ESI obtained by these three different models, assuming that even if they do not provide the exact true sources in all cases, they can convey replicable patterns that can be related to changes in measures of the clinical decline. For this purpose, we chose the SSC procedure which performs variable selection with a sparse regression method to handle high-dimensional features (Bosch-Bayard et al., 2018). In this work we tested the use of voxel-based aESI feature and ROI-based cESI and acESI, for decreasing the dimensionality but at the same time searching for increasing robustness of the spatial patterns used as features. Moreover, the SSC procedure combines the regression with resampling techniques that allow the use of non-parametric statistical evaluation of predictability but also of the stability of the variables selected. The interpretation of penalized regression is relatively straightforward and well-studied, and it is thus mostly accessible (Greenwood et al., 2020). In this sense, it is easy to see that the methodology presented here has a wider applicability and can be easily adapted to include other possible predictors and dependent measures of cognitive decline.

ESI-derived potential biomarkers of gait speed changes

With the proposed methodology, we found that the patterns selected as biomarkers of changes in GS are different according to the ESI model used. For instance, we found that the superior right frontal-orbital region appeared in biomarkers from both ENET L and NN-SLASSO, and the right precentral and postcentral regions coincide in patterns obtained with LORETA and NN-SLASSO. The NN-SLASSO model showed the best performance in terms of Inter-Class Correlation (ICC) for all ESI features, compared to the other known methods. It could be considered as a combination of Ridge L (LORETA) and LASSO with the additional sign constraint. We have observed that this method is usually sparser than ENET L and provides better localization of deep sources (Vega-Hernández et al., 2019). It is possible that the higher sparsity helps improve the predictability of the model, since the lower spatial resolution can mask different sources that provides a more informative spatial pattern. However, extremely sparse solutions can also show higher variability in the amplitude and location of the main sources, which could lead to a higher risk of overfitting and therefore lower generalization. In this sense, it is also very interesting that models obtained from NN-SLASSO also showed the higher values of replicability in comparison to the other two models. This means that the patterns of sources might be stable enough to provide a robust predictability.

The use of the connectivity ESI as a feature to predict changes in GS, we found to be more informative than the activation only ESI patterns. In all cases, the use of features including connectivity (cESI and acESI) enhanced the

predictability as measured by the ICC. The best results were obtained from acESI, i.e., when both activation and connectivity information were used as predictors, in this case by using a vector formed by the variances and absolute values of covariances among all pairs of ROIs. This result supports those previous works claiming for a leading role of the pattern of functional connections to explain changes in cognitive functions, specifically in cognitive decline related to normal and pathological aging.

In this work, the main patterns of connections that were found as potential biomarkers included the inferior temporal regions in both hemispheres, left inferior frontal triangular and right fusiform areas (with the highest replicability), as well as the connections between the left precuneus and right middle and posterior cingulate regions, in addition between left insula and left cuneus (with the highest positive regression coefficients).

To our knowledge, there are no studies in the literature that have explored the relationship between the sources of resting-state EEG and long changes of gait speed. However, there are some works that have studied the neural correlates of mobility and gait-related measures. The review carried out by Wilson et al., (2019) showed that imaging markers such as white matter integrity and cortical atrophy in frontal areas and basal ganglia were higher related to gait speed than other anatomical and functional markers. However, they did not reported results using EEG or EEG sources. Changes in EEG activity at the sensor level have been explored mainly during walking tasks, exploring increases in time-frequency activity for different bands (Huang et al., 2022) and have been even proposed to be features to classify and predict walking speed (Rahrooh, 2019).

Several researchers have looked on these neural correlates related to ageing. Sanctis et al., (2023) studied the dipole sources obtained from an independent components (IC) analysis of EEG signals recorded during walking in a treadmill in conditions of gait adjustment. Although Sanctis et al., (2023) looked at changes in predefined regions (rather than searching the whole brain) they found that individuals at higher risk for cognitive impairment amplified theta localized to the right frontal medial and central gyrus. A previous work also using sources of IC to study changes according to gait speed also found a relationship between activation in prefrontal, posterior parietal and sensorimotor networks and specific bands (Bulea et al., 2015). These authors concluded that compensatory mechanisms explain the changes in cortical activation in those elders with slow gait speed (related to cognitive impairment), which has also been supported by recent studies using NIRS activation (Greenfield et al., 2023). Despite the methodological differences with these studies, we think that our results also support this hypothesis that theta activation localized in the frontomedial cortex, may reflect higher-order compensatory responses to impairments in basic sensorimotor processes.

Finally, we also found that the levels of predictiveness achieved with our models (according to the ICC values (Koo & Li, 2016)) are in agreement with those reported in

previous studies. For instance, Babiloni et al., (2011) showed moderate AD predictivity based on source functional connectivity using the LORETA method. However, not all studies perform the same statistical assessment and therefore, although normalized, we think that the exact values of ICC should not be used as a comparable indicator of the predictive capacity of the features studied.

Limitations of the study and future work

Our work added further evidence on the usefulness of combining the activation and connectivity derived from ESI as features to predict measures related to cognitive decline. This was especially relevant when using the NN-SLASSO model for obtaining ESI and the SSC methodology to extract robust potential biomarkers. This result and the regions included in the biomarkers are strongly influenced by the ESI model and the method of selection of variables used, as mentioned above. This affects the possibility of making a fair comparison and the replicability that is expected with the previous results and among them. Future studies should address the limitations in practice to find comparable biomarkers, since selecting and comparing them requires careful consideration of various factors to ensure their robustness and generalizability. Also, further research is required to understand a more direct relation of activation and connectivity EEG as biomarkers for cognitive decline.

Although we used a validated approach to the anatomical ROI definition for specific brain areas, showing excellent longitudinal stability for multiple cortical and subcortical regions (Armstrong et al., 2019), this may also limit comparisons with other papers that use functional or any other type of ROI definitions. This is a factor that will also influence the specific results. Finally, another limitation of our study is the moderate sample size. Future studies with larger cohorts and better stratification of the sample could also be carried out in order to explore the potential of these features in a diagnostic tool for an early detection of the risk of cognitive impairment.

5. Conclusions

In this study we introduce a methodology for selecting stable biomarkers from activation and connectivity derived from Electrophysiological Source Imaging (ESI). Although the methodology is general and can be applied to any clinical, physical or cognitive measures, here we were interested in selecting those stable aESI/cESI patterns of resting-state EEG theta rhythm, as biomarkers of early cognitive decline in aging individuals reflected by a slowing of the gait speed (GS). We compared the performance of different ESI models, finding that recent proposed models that combine smoothness and sparsity with nonnegative constraints, outperformed traditional methods such as the LORETA solution in predicting changes in GS. The features combining aESI and cESI were the most stable and also provided the best prediction of GS changes. Potential biomarkers from

activation/connectivity patterns involved, orbitofrontal and temporal cortical regions, specifically the theta band.

The proposed methodology contributes to the understanding of how activity/connectivity ESI reflects the brain mechanisms underlying the changes in gait speed, providing features that are potential biomarkers of GS slowing. Given the known relationship between GS decline and cognitive impairment, this preliminary work opens novel paths to predict the progression of healthy and pathological aging and might allow an ESI-based evaluation of rehabilitation programs.

Declaration of Competing Interest

None of the authors have potential conflicts of interest to be disclosed.

Appendix A. Supplementary material

The online supplementary material contains complementary details on the real data results.

References

- Afilalo, J., Kim, S., Brien, S. O., Brennan, J. M., Edwards, F. H., Mack, M. J., McClurken, J. B., Jr, J. C. C., Smith, P. K., Shahian, D. M., & Alexander, K. P. (2016). Gait Speed and Operative Mortality in Older Adults Following Cardiac Surgery. *JAMA Cardiology*, *1*(3), 314–321. <https://doi.org/10.1001/jamacardio.2016.0316>
- Armstrong, N. M., An, Y., Beason-held, L., Doshi, J., Erus, G., Ferrucci, L., Davatzikos, C., & Resnick, S. M. (2019). Neurobiology of Aging Sex differences in brain aging and predictors of neurodegeneration in cognitively healthy older adults. *Neurobiology of Aging*, *81*, 146–156. <https://doi.org/10.1016/j.neurobiolaging.2019.05.020>
- Babiloni, C., Del, C., Lizio, R., Noce, G., Lopez, S., Soricelli, A., Ferri, R., Teresa, M., Catania, V., Nobili, F., Arnaldi, D., Famà, F., Orzi, F., Buttinelli, C., Giubilei, F., Bonanni, L., Franciotti, R., Onofri, M., Stirpe, P., ... Stocchi, F. (2018). *Clinical Neurophysiology Functional cortical source connectivity of resting state electroencephalographic alpha rhythms shows similar abnormalities in patients with mild cognitive impairment due to Alzheimer 's and Parkinson 's diseases*. *129*, 766–782. <https://doi.org/10.1016/j.clinph.2018.01.009>
- Babiloni, C., Vecchio, F., Lizio, R., Ferri, R., & Rodriguez, G. (2011). *Resting State Cortical Rhythms in Mild Cognitive Impairment and Alzheimer 's Disease : Electroencephalographic Evidence*. *26*, 201–214. <https://doi.org/10.3233/JAD-2011-0051>
- Bosch-Bayard, J., Galán-García, L., Fernandez, T., Lirio, R. B., Bringas-Vega, M. L., Roca-Stappung, M., Ricardo-Garcell, J., Harmony, T., & Valdes-Sosa, P. A. (2018). Stable Sparse Classifiers Identify qEEG Signatures that Predict Learning Disabilities (NOS) Severity. *Front. Neurosci*, *11*(January), 749. <https://doi.org/10.3389/fnins.2017.00749>
- Bosch-Bayard, J., Valdés-Sosa, P. A., Virues-Alba, T., Aubert-Vázquez, E., Roy John, E., Harmony, T., Riera-Díaz, J., & Trujillo-Barreto, N. (2001). 3D Statistical Parametric Mapping of EEG Source Spectra by Means of Variable Resolution Electromagnetic Tomography (VARETA). *Clinical Electroencephalography*, *32*(2), 47–66.
- Bressler, S. L., & Menon, V. (2010). Large-scale brain networks in cognition : emerging methods and principles. *Trends in Cognitive Sciences*, *14*(6), 277–290. <https://doi.org/10.1016/j.tics.2010.04.004>
- Bulea, T. C., Kim, J., Damiano, D. L., Stanley, C. J., & Park, H. (2015). Prefrontal , posterior parietal and sensorimotor network activity

- underlying speed control during walking. *Frontiers in Human Neuroscience*, 9(May), 1–13. <https://doi.org/10.3389/fnhum.2015.00247>
- Cohen, J. A., & Verghese, J. (2019). Gait and dementia. In S. T. D. and S. Asthana (Ed.), *Handbook of Clinical Neurology, Geriatric Neurology* (1st ed., Vol. 167, pp. 419–427). Elsevier B.V. <https://doi.org/10.1016/B978-0-12-804766-8.00022-4>
- Collyer, T. A., Murray, A. M., Woods, R. L., Storey, E., Chong, T. T., & Ryan, J. (2022). Association of Dual Decline in Cognition and Gait Speed With Risk of Dementia in Older Adults. 5(5), 1–13. <https://doi.org/10.1001/jamanetworkopen.2022.14647>
- Cozac, V. V., Gschwandtner, U., Hatz, F., Hardmeier, M., Rüegg, S., & Fuhr, P. (2016). *Quantitative EEG and Cognitive Decline in Parkinson's Disease*. 2016(d).
- Darweesh, S. K. L., Licher, S., Wolters, F. J., Koudstaal, P. J., Ikram, M. K., & Ikram, M. A. (2019). Quantitative gait, cognitive decline, and incident dementia: The Rotterdam Study. *Alzheimer's & Dementia*, 1–10. <https://doi.org/10.1016/j.jalz.2019.03.013>
- De Sanctis, P., Wagner, J., Molholm, S., Foxe, J. J., Blumen, H. M., & Horsthuis, D. J. (2023). Neural signature of mobility-related everyday function in older adults at-risk of cognitive impairment. 122, 1–11. <https://doi.org/10.1016/j.neurobiolaging.2022.11.005>
- Dumurgier, J., Artaud, F., Touraine, C., Rouaud, O., Tavernier, B., Dufouil, C., Singh-manoux, A., Tzourio, C., Elbaz, A., Inerm, U., Hospital, L., & Paré, A. (2017). Gait Speed and Decline in Gait Speed as Predictors of Incident Dementia Editor's Choice. 72(5), 655–661. <https://doi.org/10.1093/gerona/glw110>
- Fritz, S., & Lusardi, M. (2009). White Paper: "Walking Speed: the Sixth Vital Sign." *Journal of Geriatric Physical Therapy*, 32(2), 2–5.
- García-Agustín, D., Morgade-Fonte, R. M., Bobes, M. A., García, L. G., & Rodríguez-Rodríguez, V. (2020). Association between gait speed decline and EEG abnormalities in a cohort of active older adults living in the community. 3–9. <https://doi.org/https://doi.org/10.1101/2020.05.03.20089540>
- Greenfield, J., Delcroix, V., Ettaki, W., Derollepot, R., Paire-ficout, L., & Ranchet, M. (2023). Left and Right Cortical Activity Arising from Preferred Walking Speed in Older Adults. *Sensors*, 23(3986). <https://doi.org/https://doi.org/10.3390/s23083986>
- Greenwood, C. J., Youssef, G. J., Letcher, P., Macdonald, J. A., Hagg, L. J., Sanson, A., McIntosh, J., Delyse, Hutchinson, M., Toumbourou, J. W., Fuller-Tyszkiewicz, M., & Olsson, C. A. (2020). A comparison of penalised regression methods for informing the selection of predictive markers. *PLoS ONE*, 15(11), 1–14. <https://doi.org/10.1371/journal.pone.0242730>
- Hata, M., Kazui, H., Tanaka, T., Ishii, R., Canuet, L., Pascual-Marqui, R. D., Aoki, Y., Ikeda, S., Kanemoto, H., Yoshiyama, K., Iwase, M., & Takeda, M. (2016). Functional connectivity assessed by resting state EEG correlates with cognitive decline of Alzheimer's disease - An eLORETA study. *Clinical Neurophysiology*, 127(2), 1269–1278. <https://doi.org/10.1016/j.clinph.2015.10.030>
- Hata, M., Tanaka, T., Kazui, H., Ishii, R., Canuet, L., Pascual-marqui, R. D., Aoki, Y., Ikeda, S., Sato, S., Suzuki, Y., Kanemoto, H., Yoshiyama, K., & Iwase, M. (2017). Cerebrospinal Fluid Biomarkers of Alzheimer's Disease Correlate With Electroencephalography Parameters Assessed by Exact Low-Resolution Electromagnetic Tomography (eLORETA). *Clinical EEG and Neuroscience*, 48(5), 338–347. <https://doi.org/10.1177/1550059416662119>
- Haufe, S., Nikulin, V. V., Ziehe, A., Müller, K. R., & Nolte, G. (2008). Combining sparsity and rotational invariance in EEG/MEG source reconstruction. *NeuroImage*, 42(2), 726–738. <https://doi.org/10.1016/j.neuroimage.2008.04.246>
- Haufe, S., Tomioka, R., Dickhaus, T., Sannelli, C., Blankertz, B., Nolte, G., & Müller, K. (2011). NeuroImage Large-scale EEG / MEG source localization with spatial flexibility. *NeuroImage*, 54(2), 851–859. <https://doi.org/10.1016/j.neuroimage.2010.09.003>
- He, B., Astolfi, L., Valdés-sosa, P. A., Marinazzo, D., Palva, S. O., Michel, C. M., & Koenig, T. (2019). Electrophysiological Brain Connectivity: Theory and Implementation. *IEEE TRANSACTIONS ON BIOMEDICAL ENGINEERING*, 66(7), 2115–2135. <https://doi.org/10.1109/TBME.2019.2913928>
- Horwitz, B. (2003). The elusive concept of brain connectivity. *NeuroImage*, 19(2), 466–470. [https://doi.org/10.1016/S1053-8119\(03\)00112-5](https://doi.org/10.1016/S1053-8119(03)00112-5)
- Huang, C.-Y., Chen, Y.-A., Wu, R.-M., & Hwang, I.-S. (2022). Dual-task walking improvement with enhanced kinesthetic awareness in Parkinson's disease with mild gait impairment: EEG connectivity and clinical implication. *Frontiers in Aging Neuroscience*, 14(November), 1–13. <https://doi.org/10.3389/fnagi.2022.1041378>
- Huang, H., Condor, A., & Huang, H. J. (2020). Classification of EEG Motion Artifact Signals Using Spatial ICA Classification of EEG Motion Artifact Signals Using Spatial ICA. In D.-G. (Din) Chen (Ed.), *Statistical Modeling in Biomedical research* (Issue March, pp. 23–35). <https://doi.org/10.1007/978-3-030-33416-1>
- Jabès, A., Klencklen, G., Ruggeri, P., Antonietti, J. P., Banta Lavenex, P., & Lavenex, P. (2021). Age-Related Differences in Resting-State EEG and Allocentric Spatial Working Memory Performance. *Frontiers in Aging Neuroscience*, 13(November). <https://doi.org/10.3389/fnagi.2021.704362>
- Jovicich, J., Barkhof, F., Babiloni, C., Herholz, K., Mulert, C., van Berckel, B. N. M., & Frisoni, G. B. (2019). Harmonization of neuroimaging biomarkers for neurodegenerative diseases: A survey in the imaging community of perceived barriers and suggested actions. *Alzheimer's and Dementia: Diagnosis, Assessment and Disease Monitoring*, 11, 69–73. <https://doi.org/10.1016/j.dadm.2018.11.005>
- Kahya, M., Moon, S., Ranchet, M., Vukas, R. R., Lyons, K. E., Pahwad, R., Akinwuntana, A., & Devos, H. (2019). Brain activity during dual task gait and balance in aging and age-related neurodegenerative conditions: A systematic review Brain activity during dual task gait and balance in aging and age-related neurodegenerative conditions: A systematic review. *Experimental Gerontology*, 128(November), 110756. <https://doi.org/10.1016/j.exger.2019.110756>
- Kim, B., Yu, D., & Won, J.-H. (2018). Comparative study of computational algorithms for the Lasso with high-dimensional, highly correlated data. *Appl Intell*, 48, 1933–1952. <https://doi.org/10.1007/s10489-016-0850-7>
- Knösche, T. R., & Haueisen, J. (2022). *EEG / MEG Source Reconstruction*. Springer Nature Switzerland AG.
- Koo, T. K., & Li, M. Y. (2016). A Guideline of Selecting and Reporting Intraclass Correlation Coefficients for Reliability Research. *Journal of Chiropractic Medicine*, 15(2), 155–163. <https://doi.org/10.1016/j.jcm.2016.02.012>
- Li, M., Wang, Y., Lopez-Naranjo, C., Hu, S., Reyes, R. C. G., Paz-Linares, D., Areces-Gonzalez, A., Hamid, A. I. A., Evans, A. C., Savostyanov, A. N., Calzada-Reyes, A., Villringer, A., Tobon-Quintero, C. A., Garcia-Agustin, D., Yao, D., Dong, L., Aubert-Vazquez, E., Reza, F., Razaq, F. A., ... Valdés-Sosa, P. A. (2022). Harmonized-Multinational qEEG norms (HarMNqEEG). *NeuroImage*, 256(March), 119190. <https://doi.org/10.1016/j.neuroimage.2022.119190>
- Liljequist, D., Elfving, B., & Roaldsen, K. S. (2019). Intraclass correlation – A discussion and demonstration of basic features. *PLoS ONE*, 14(7), e0219854. <https://doi.org/10.1371/journal.pone.0219854>
- Marinazzo, D., Riera, J. J., Marzetti, L., Astolfi, L., Yao, D., & Valdés Sosa, P. A. (2019). Controversies in EEG Source Imaging and Connectivity: Modeling, Validation, Benchmarking. *Brain Topography*, 32(4), 527–529. <https://doi.org/10.1007/s10548-019-00709-9>
- Meghdadi, A. H., Karic, M. S., McConnell, M., Rupp, G., Richard, C., Hamilton, J., Salat, D., & Berka, C. (2021). Resting state EEG biomarkers of cognitive decline associated with Alzheimer's disease and mild cognitive impairment. *PLoS ONE*, 16(2 February), 1–31. <https://doi.org/10.1371/journal.pone.0244180>
- Min, J. Y., Ha, S. W., Lee, K., & Min, K. B. (2022). Use of electroencephalogram, gait, and their combined signals for classifying cognitive impairment and normal cognition. *Frontiers in Aging Neuroscience*, 14(September), 1–12. <https://doi.org/10.3389/fnagi.2022.927295>
- Montero-odasso, M., Speechley, M., Muir-hunter, S. W., Pieruccini-faria, F., Sarquis-adamson, Y., Hachinski, V., Bherer, L., Borrie, M., Wells, J., Garg, A. X., Tian, Q., Ferrucci, L., Bray, N. W., Cullen, S., Mahon, J., Titus, J., & Camicioli, R. (2020). *Dual decline in*

- gait speed and cognition is associated with future dementia : *June*, 995–1002. <https://doi.org/10.1093/ageing/afaa106>
- Musaeus, C. S., Engedal, K., Høgh, P., Jelic, V., Mørup, M., Naik, M., Anne-Rita Oeksengaard, J. S., Lars-Olof Wahlund, Waldemar, G., & Andersen, B. B. (2018). EEG Theta Power Is an Early Marker of Cognitive Decline in Dementia due to Alzheimer's Disease. *Journal of Alzheimer's Disease*, 64(4), 1359–1371. <https://doi.org/10.3233/JAD-180300>
- Muthuraman, Hellriegel, H., Hoogenboom, N., Anwar, A. R., Mideksa, K. G., Krause, H., Schnitzler, A., Deuschl, G., & Raethjen, J. (2014). Beamformer source analysis and connectivity on concurrent EEG and MEG data during voluntary movements. *PLoS ONE*, 9(3). <https://doi.org/10.1371/journal.pone.0091441>
- Nascimento, M. D. M., Gouveia, É. R., Marques, A., Gouveia, B. R., Marconcin, P., & Ihle, A. (2022). Gait Speed as a Biomarker of Cognitive Vulnerability: A Population-Based Study with Cognitively Normal Older Adults. *Sustainability*, 14(12), 7348. <https://doi.org/10.3390/su14127348>
- Nordin, A. D., Hairston, W. D., & Ferris, D. P. (2020). Faster Gait Speeds Reduce Alpha and Beta EEG Spectral Power from Human Sensorimotor Cortex. *IEEE Transactions on Biomedical Engineering*, 67(3), 842–853. <https://doi.org/10.1109/TBME.2019.2921766>
- Öhlin, J., Ahlgren, A., Folkesson, R., Gustafson, Y., Littbrand, H., & Olofsson, B. (2020). *The association between cognition and gait in a representative sample of very old people – the influence of dementia and walking aid use*. 1–10.
- Pascual-Marqui, R. D. (2002). Standardized low resolution brain electromagnetic tomography (sLORETA): technical details. *Methods & Findings in Experimental & Clinical Pharmacology*, 24(D), 5–12. <https://doi.org/841> [pii]
- Pascual-Marqui, R. D. (2007). *Discrete, 3D distributed linear imaging methods of electric neuronal activity. Part I: exact, zero error localization*. 1–16.
- Pascual-Marqui, R. D., Michel, C. M., & Lehmann, D. (1994). Low resolution electromagnetic tomography: a new method for localizing electrical activity in the brain. *International Journal of Psychophysiology*, 18, 49–65.
- Paz-Linares, D., Gonzalez-Moreira, E., Areces-Gonzalez, A., Wang, Y., Li, M., Vega-Hernandez, M., Wang, Q., Bosch-Bayard, J., Bringas-Vega, M. L., Martínez-Montes, E., Valdes-Sosa, M. J., & Valdes-Sosa, P. A. (2023). Minimizing the distortions in electrophysiological source imaging of cortical oscillatory activity via Spectral Structured Sparse Bayesian Learning. *Frontiers in Neuroscience*, 17, 978527. <https://doi.org/10.3389/fnins.2023.978527>
- Peters, D. M., Fritz, S. L., & Krotish, D. E. (2013). *Assessing the Reliability and Validity of a Shorter Walk Test Compared With the 10-Meter Walk Test for Measurements of Gait Speed in Healthy, Older Adults*. 36(1). <https://doi.org/10.1519/JPT.0b013e318248e20d>
- Prichep, L. S. (2007). *Quantitative EEG and Electromagnetic Brain Imaging in Aging and in the*. 167, 156–167. <https://doi.org/10.1196/annals.1379.008>
- Prichep, L. S., John, E. R., Ferris, S. H., Rausch, L., Fang, Z., Cancro, R., Torossian, C., & Reisberg, B. (2005). *Prediction of longitudinal cognitive decline in normal elderly with subjective complaints using electrophysiological imaging*. <https://doi.org/10.1016/j.neurobiolaging.2005.07.021>
- Rahroo, A. (2019). *Classifying and Predicting Walking Speed From Electroencephalography Data*.
- Riera, J. J., & Fuentes, M. E. (1998). Electric Lead Field for a Piecewise Homogeneous Volume Conductor Model of the Head. *IEEE TRANSACTIONS ON BIOMEDICAL ENGINEERING*, 45(6), 746–753. <https://doi.org/10.1109/10.678609>
- Skillbäck, T., Blennow, K., Zetterberg, H., Skoog, J., Rydén, L., Wetterberg, H., Guo, X., Sacuiu, S., Mielke, M. M., Zettergren, A., Skoog, I., & Kern, S. (2021). Slowing gait speed precedes cognitive decline by several years. *Alzheimer's and Dementia*, 18(9), 1667–1676. <https://doi.org/10.1002/alz.12537>
- Smailovic, U., & Jelic, V. (2019). Neurophysiological Markers of Alzheimer's Disease : Quantitative EEG Approach. *Neurology and Therapy*, 8(s2), 37–55. <https://doi.org/10.1007/s40120-019-00169-0>
- Smailovic, U., Koenig, T., Kåreholt, I., Andersson, T., Kramberger, M. G., Winblad, B., & Jelic, V. (2018). Quantitative EEG power and synchronization correlate with Alzheimer's disease CSF biomarkers. *Neurobiology of Aging*, 63, 88–95. <https://doi.org/10.1016/j.neurobiolaging.2017.11.005>
- Sohrabpour, A., Member, S., Ye, S., Worrell, G. A., Zhang, W., & He, B. (2016). *Noninvasive Electromagnetic Source Imaging and Granger Causality Analysis : An Electrophysiological Connectome (eConnectome) Approach*. 63(12), 2474–2487.
- Tibshirani, R. (1996). Regression Selection and Shrinkage via the Lasso. In *Journal of the Royal Statistical Society B* (Vol. 58, Issue 1, pp. 267–288). <https://doi.org/10.2307/2346178>
- Tzema-shahar, R., Hochner, H., Iktilat, K., & Agmon, M. (2022). What can we learn from physical capacity about biological age ? A systematic review. *Ageing Research Reviews*, 77(March), 101609. <https://doi.org/10.1016/j.arr.2022.101609>
- Tzourio-Mazoyer, N., Landeau, B., Papathanassiou, D., Crivello, F., Etard, O., Delcroix, N., Mazoyer, B., & Joliot, M. (2002). Automated anatomical labeling of activations in SPM using a macroscopic anatomical parcellation of the MNI MRI single-subject brain. *NeuroImage*, 15(1), 273–289. <https://doi.org/10.1006/nimg.2001.0978>
- Van de Steen, F., Almgren, H., Razi, A., Friston, K., & Marinazzo, D. (2019). Dynamic causal modelling of fluctuating connectivity in resting-state EEG. *NeuroImage*, 189(January), 476–484. <https://doi.org/10.1016/j.neuroimage.2019.01.055>
- Van de Steen, F., Faes, L., Karahan, E., Songsiri, J., Valdes-Sosa, P. A., & Marinazzo, D. (2019). Critical Comments on EEG Sensor Space Dynamical Connectivity Analysis. *Brain Topography*, 32(4), 643–654. <https://doi.org/10.1007/s10548-016-0538-7>
- Vecchio, D. F., Miraglia, D. F., Iberite, D. F., Lacidogna, D. G., Guglielmi, D. V., Marra, D. C., Pasqualetti, D. P., Tiziano, D. F. D., & Rossini, P. P. M. (2018). Sustainable method for Alzheimer dementia prediction in mild cognitive impairment: Electroencephalographic connectivity and graph theory combined with apolipoprotein E. *Annals of Neurology*, 84(2), 302–314. <https://doi.org/10.1002/ana.25289>
- Vega-Hernández, M., Martínez-Montes, E., Sánchez-Bornot, J. M., Lage-Castellanos, A., & Valdés-Sosa, P. A. (2008). Penalized Least Squares methods for solving the EEG Inverse Problem. *Statistica Sinica*, 18(4).
- Vega-Hernández, M., Palmero-Ledón, D., Sánchez-Bornot, J. M., Pérez-Hidalgo-Gato, J., García-Agustín, D., Valdés-Sosa, P. A., & Martínez-Montes, E. (2022). Finding electrophysiological sources of aging-related processes using penalized least squares with a Modified Newton-Raphson algorithm. *Rev. CENIC Cienc. Biol.*, 53(2), 219–242.
- Vega-Hernández, M., Sánchez-Bornot, J. M., Pérez-Hidalgo-Gato, J., Alvarez Iglesias, J. E., Martínez-Montes, E., & Valdés-Sosa, P. A. (2019). Penalized least squares and sign constraints with modified Newton-Raphson algorithms: Application to EEG source imaging. <https://arxiv.org/abs/1911.01961v4>
- Voelcker-rehage, C., Godde, B., & Staudinger, U. M. (2011). *Cardiovascular and coordination training differentially improve cognitive performance and neural processing in older adults*. 5(March), 1–12. <https://doi.org/10.3389/fnhum.2011.00026>
- Wilson, J., Allcock, L., Mc Ardle, R., Taylor, J. P., & Rochester, L. (2019). The neural correlates of discrete gait characteristics in ageing: A structured review. In *Neuroscience and Biobehavioral Reviews* (Vol. 100, Issue December 2018, pp. 344–369). Elsevier. <https://doi.org/10.1016/j.neubiorev.2018.12.017>
- Zhou, H., Shahbazi, M., & York, K. (2021). *Digital Biomarkers of Cognitive Frailty : The Value of Detailed Gait Assessment Beyond Gait Speed*. <https://doi.org/10.1159/000515939>
- Zou, H., & Hastie, T. (2005). Regularization and variable selection via the elastic-net. *Journal of the Royal Statistical Society*, 67(1), 301–320. <https://doi.org/10.1111/j.1467-9868.2005.00503.x>

SUPPLEMENTAL MATERIAL

Predicting aging-related decline in physical performance with sparse electrophysiological source imaging.

Vega-Hernández, Mayrim^{1,2}, Galán-García, Lídice², Pérez-Hidalgo-Gato, Jhoanna², Ontivero-Ortega, Marlis², García-Reyes, Ronaldo², Bosch-Bayard, Jorge³, Martínez-Montes, Eduardo^{2,*}, Marinazzo, Daniele⁴ and Valdés-Sosa, Pedro A.^{1,2,*}

¹The Clinical Hospital of Chengdu Brain Science Institute, MOE Key Lab for Neuroinformatics, University of Electronic Science and Technology of China, Chengdu, China.

²Cuban Center for Neurosciences, Havana, Cuba.

³Montreal Neurological Institute, Canada.

⁴Faculty of Psychology and Educational Sciences, Department of Data Analysis, Ghent University.

* Corresponding author at:

Cuban Center for Neurosciences, Human Brain Mapping Division, Havana, Cuba.

The Clinical Hospital of Chengdu Brain Science Institute, MOE Key Lab for Neuroinformatics, University of Electronic Science and Technology of China, Chengdu, China.

E-mail address: eduardo@cneuro.edu.cu; pedro.valdes@neuroinformatics-collaboratory.org.

This work was supported by the VLIR-UOS project “A Cuban National School of Neurotechnology for Cognitive Aging” and the National Fund for Science and Innovation of Cuba. CU2017TEA436A103. Partial funding was also provided by the Cuban National Program for Neuroscience and Neurotechnology, Project “Development of disease progression models for brain dysfunctions” PN305LH013-015.

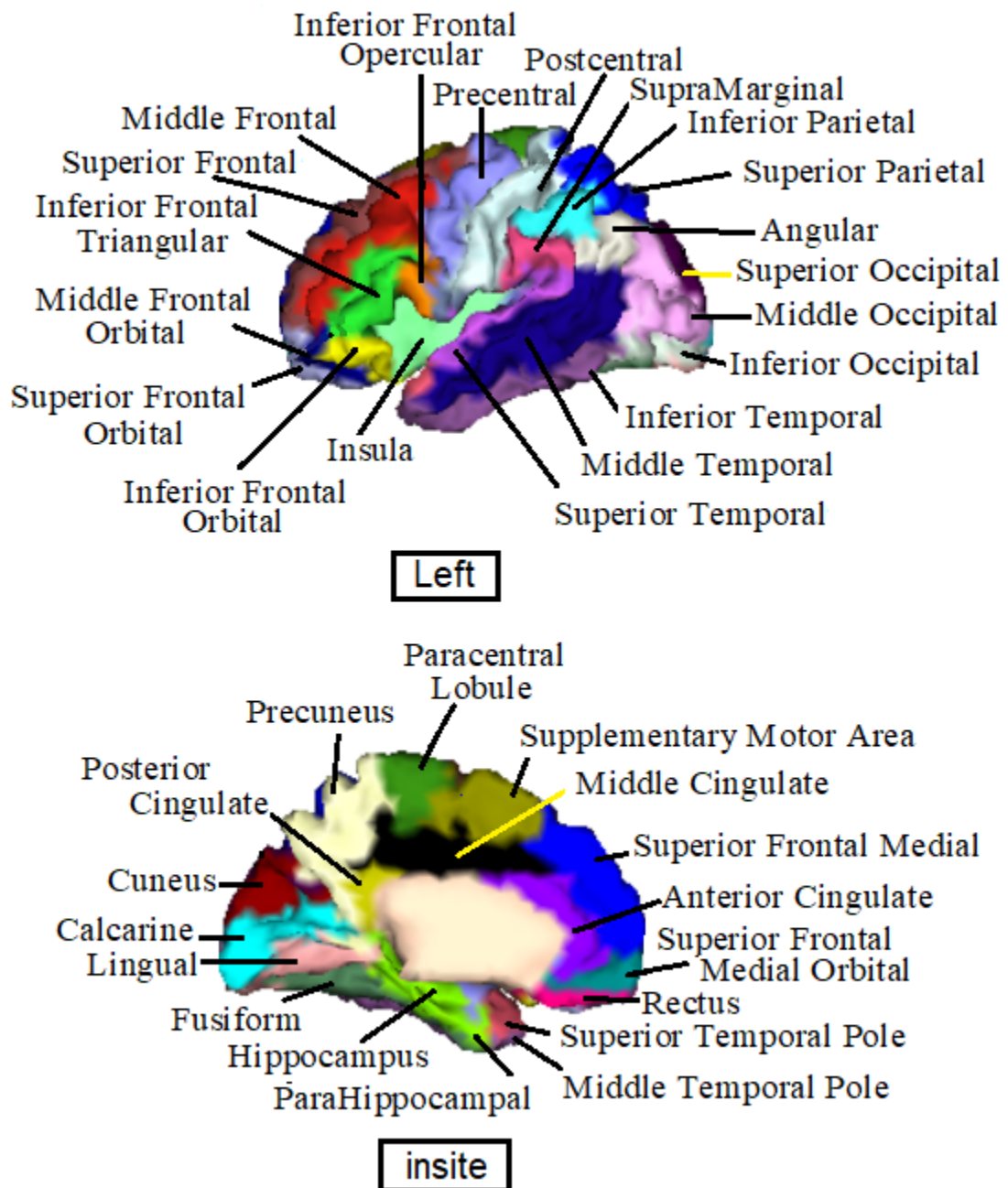


Fig. S1: Set of 76 nodes (including left and right hemispheres, as showing in Table S1) selected from anatomical compartments included in the segmentation of the Automated Anatomical Labeling (AAL) average brain of the Montreal Neurological Institute (Tzourio-Mazoyer et al. 2002)

Table S1. Index of the 76 cortical labels extracted from the segmentation of the Automated Anatomical Labeling (AAL) average brain of the Montreal Neurological Institute.

Name	Label	Hemisphere		Name	Label	Hemisphere	
		Left	Right			Left	Right
Precentral	PRE	1	2	Calcarine	VI	39	40
Superior Frontal	SF	3	4	Cuneus	Q	41	42
Superior Frontal Orbital	SFOrb	5	6	Lingual	LING	43	44
Middle Frontal	MF	7	8	Superior Occipital	SO	45	46
Middle Frontal Orbital	MFOrb	9	10	Middle Occipital	MO	47	48
Inferior Frontal Opercular	IFOp	11	12	Inferior Occipital	IO	49	50
Inferior Frontal Triangular	IFTri	13	14	Fusiform	FUSI	51	52
Inferior Frontal Orbital	IFOrb	15	16	Postcentral	POST	53	54
Rolandic Operculum	RO	17	18	Superior Parietal	SP	55	56
Supplementary Motor Area	SMA	19	20	Inferior Parietal	IP	57	58
Superior Frontal Medial	SFMed	21	22	SupraMarginal	SM	59	60
Superior Frontal Medial Orbital	SFMedOrb	23	24	Angular	A	61	62
Rectus	R	25	26	Precuneus	PQ	63	64
Insula	IN	27	28	Paracentral Lobule	PCL	65	66
Anterior Cingulate	AC	29	30	Superior Temporal	ST	67	68
Middle Cingulate	MC	31	32	Superior Temporal Pole	STP	69	70
Posterior Cingulate	PC	33	34	Middle Temporal	MT	71	72
Hippocampus	HIP	35	36	Middle Temporal Pole	MTP	73	74
ParaHippocampal	PHIP	37	38	Inferior Temporal	IT	75	76

Table S2. ROIs with significant correlation with GS.

	#	Label	ROI Name	Correlation
LORETA	44	LING	Lingual Right	-0.3147
	57	IP	Inferior Parietal left	0.2736
	59	SM	SupraMarginal left	0.2708
	53	POST	Postcentral left	0.2549
	55	SP	Superior Parietal left	0.2562
	50	IO	Inferior Occipital Right	-0.2434
	18	RO	Rolandic Operculum Right	0.2383
	61	A	Angular left	0.2374
	54	POST	Postcentral Right	0.2314
	2	PRE	Precentral Right	0.2200
	63	PQ	Precuneus left	0.2157
	65	PCL	Paracentral Lobule left	0.2153
	67	ST	Superior Temporal left	0.2151
ENET L	38	PHIP	ParaHippocampal Right	-0.3492
	72	MT	Middle Temporal Right	-0.3067
	52	FUSI	Fusiform Right	-0.2971
	36	HIP	Hippocampus Right	-0.2906
	74	MTP	Middle Temporal Pole Right	-0.2353
	26	R	Rectus Right	-0.2330
	6	SFOrb	Superior Frontal Orbital Right	-0.2194
NN-SLASSO	75		Inferior Temporal left	0.3230
	6	SFOrb	Superior Frontal Orbital Right	-0.2590
	54	POST	Postcentral Right	-0.2300
	76	IT	Inferior Temporal Right	0.2293
	10	MFOrb	Middle Frontal Orbital Right	-0.2253
	30	AC	Anterior Cingulate Right	-0.2112
	2	PRE	Precentral Right	0.2033

Table S3. Performance of models for each feature (aESI, cESI, acESI) and each method (LORETA, ENET L, NN-SLASSO) tested

Method	Feature	ICC	ICC-IC	p-value	F	R	p
LORETA	aESI	0.2220	[0.0184 0.4384]	0.0349	1.5706	0.15	0.0021
	cESI	0.4508	[0.2371 0.6232]	5.9468e-05	2.6418	0.33	0.0000
	acESI	0.4967	[0.2921 0.6581]	8.6236e-06	2.9738	0.37	0.0000
ENET L	aESI	0.2029	[0.0383 0.4222]	0.0490	1.5092	0.15	0.0032
	cESI	0.2629	[0.0252 0.4729]	0.0154	1.7134	0.26	0.0000
	acESI	0.3009	[0.0663 0.5043]	0.0065	1.8608	0.27	0.0000
NN-SLASSO	aESI	0.4016	[0.1795 0.5850]	0.0004	2.3423	0.29	0.0000
	cESI	0.6545	[0.4923 0.7730]	7.6453e-10	4.7884	0.59	0.0000
	acESI	0.6878	[0.5369 0.7963]	4.9805e-11	5.4068	0.62	0.0000

Table S4. Selected models based on aESI feature estimated by NN-SLASSO method.

aESI			
#	ROI Name	Replicability	Beta in Best Model
75	Inferior Temporal Left	58,38	0,42
54	Postcentral Right	42,50	-0,20
76	Inferior Temporal Right	41,21	0,23
6	Superior Frontal Orbital Right	41,18	-0,36

Table S5. Selected models based on cESI feature estimated by NN-SLASSO method.

cESI			
Name ROI 1	Name ROI 2	Replicability	Beta in Best Model
Middle Cingulate Right	Precuneus Left	20,11	13,95
Posterior Cingulate Right	Paracentral Lobule Left	20,59	6,01
Posterior Cingulate Right	Precuneus Left	26,28	4,67
Insula Left	Cuneus Left	22,31	1,57
Middle Cingulate Left	Paracentral Lobule Left	21,01	1,11
Middle Cingulate Right	Inferior Temporal Left	22,25	0,86
Posterior Cingulate Left	Inferior Temporal Left	24,37	0,79
Posterior Cingulate Left	Fusiform Left	24,07	0,59
Middle Cingulate Left	Inferior Temporal Left	20,93	0,51
Rolandic Operculum Left	Middle Temporal Right	22,35	0,30

Inferior Frontal Orbital Right	Inferior Temporal Left	27,03	0,27
Inferior Frontal Opercular Left	Insula Right	20,46	0,27
Inferior Frontal Triangular Left	Fusiform Right	47,73	0,27
Anterior Cingulate Left	Inferior Temporal Left	23,01	0,24
Inferior Frontal Orbital Left	Lingual Left	22,10	0,22
Insula Right	Fusiform Left	30,53	0,22
Inferior Frontal Opercular Left	Middle Temporal Left	36,81	0,21
Rectus Left	Middle Temporal Right	22,74	0,20
Inferior Temporal Left	Inferior Temporal Right	49,57	0,20
Inferior Frontal Triangular Right	Middle Temporal Pole Left	30,14	0,19
Inferior Frontal Orbital Left	Inferior Temporal Right	46,31	0,18
Middle Temporal Right	Inferior Temporal Left	49,58	0,17
Middle Frontal Orbital Left	Inferior Temporal Right	25,49	0,17
Middle Frontal Orbital Left	Inferior Temporal Left	35,93	0,16
Middle Frontal Left	Superior Temporal Right	29,04	0,16
Middle Frontal Left	Middle Temporal Right	38,32	0,15
Inferior Occipital Left	Superior Temporal Right	23,38	0,15
Middle Temporal Pole Left	Inferior Temporal Right	31,58	0,15
Inferior Frontal Orbital Right	Inferior Temporal Right	23,60	0,15
Superior Frontal Orbital Left	Inferior Temporal Right	22,25	0,14
Anterior Cingulate Left	Middle Temporal Right	21,08	0,14
Inferior Frontal Opercular Left	Inferior Temporal Left	33,43	0,14
Superior Temporal Right	Inferior Temporal Right	24,43	0,13
Inferior Frontal Triangular Right	Inferior Temporal Left	38,62	0,13
Lingual Left	Inferior Temporal Right	36,84	0,13
ParaHippocampal Left	Inferior Occipital Left	22,10	0,13
Inferior Occipital Left	Inferior Temporal Right	43,91	0,12
Middle Frontal Orbital Left	Inferior Temporal Right	33,53	0,12
Inferior Frontal Triangular Left	Inferior Temporal Right	43,79	0,11
Inferior Occipital Right	Middle Temporal Left	27,79	0,11
Inferior Occipital Right	Inferior Parietal Right	22,29	0,11
Middle Occipital Right	Inferior Occipital Right	23,35	0,11
Inferior Frontal Triangular Left	Middle Temporal Right	46,15	0,11

Inferior Frontal Triangular Left	Middle Temporal Left	32,01	0,11
Superior Temporal Right	Inferior Temporal Left	24,93	0,11
Inferior Frontal Opercular Left	Middle Temporal Right	30,14	0,11
Lingual Left	Middle Temporal Right	38,20	0,11
Middle Frontal Left	Inferior Temporal Left	32,49	0,10
Inferior Frontal Orbital Left	Middle Temporal Right	30,54	0,10
Inferior Frontal Orbital Right	Inferior Occipital Left	21,67	0,10
Inferior Frontal Triangular Left	Lingual Right	28,32	0,10
Inferior Frontal Triangular Left	Superior Temporal Right	25,80	0,10
Lingual Left	Inferior Temporal Left	28,53	0,10
Inferior Frontal Orbital Right	Fusiform Left	20,56	0,10
Calcarine Right	Inferior Temporal Left	28,33	0,10
Middle Temporal Left	Inferior Temporal Right	32,26	0,10
Inferior Frontal Triangular Left	Inferior Occipital Right	51,04	0,10
Middle Occipital Left	Inferior Occipital Right	31,21	0,09
Middle Occipital Left	Inferior Temporal Left	35,94	0,09
Inferior Frontal Triangular Left	Inferior Temporal Left	34,69	0,09
Fusiform Right	Middle Temporal Left	25,95	0,09
Middle Frontal Orbital Left	Middle Temporal Right	24,50	0,09
Superior Temporal Left	Inferior Temporal Right	30,19	0,08
Inferior Frontal Orbital Left	Inferior Occipital Right	23,91	0,08
Inferior Frontal Opercular Left	Inferior Temporal Right	28,65	0,08
Middle Frontal Orbital Left	Inferior Occipital Left	28,99	0,08
Middle Frontal Left	Inferior Temporal Right	26,27	0,07
Inferior Frontal Tri Left	Lingual Left	30,81	0,07
Middle Occipital Right	Middle Temporal Left	23,93	0,07
Calcarine Left	Inferior Temporal Right	24,86	0,07
Inferior Frontal Opercular Left	Calcarine Right	23,14	0,07
Middle Occipital Left	Inferior Temporal Right	26,68	0,06
Inferior Occipital Left	Middle Temporal Right	41,41	0,06
Fusiform Right	Inferior Temporal Right	26,55	0,06
Middle Temporal Left	Inferior Temporal Left	31,88	0,06
Fusiform Left	Inferior Temporal Left	30,84	0,06
Inferior Occipital Left	Inferior Temporal Left	48,71	0,05
Middle Occipital Left	Middle Temporal Left	23,10	0,05

Middle Temporal Right	Inferior Temporal Right	31,55	0,05
Middle Occipital Left	Middle Temporal Right	23,65	0,05
Inferior Frontal Triangular Left	Calcarine Left	20,29	0,05
Fusiform Right	Inferior Temporal L'	28,69	0,05
Inferior Frontal Triangular Right	Inferior Temporal Right	25,94	0,05
Inferior Frontal Opercular Left	Inferior Occipital Right	31,84	0,04
Middle Frontal Left	Inferior Occipital Left	21,73	0,03
ParaHippocampal Left	Fusiform Left	23,63	0,03
Fusiform Right	Middle Temporal Right	21,10	0,03
Inferior Frontal Tri Left	Fusiform Left	35,08	0,03
Inferior Occipital Right	Inferior Temporal Left	37,08	0,03
Lingual Left	Inferior Occipital Left	23,10	0,03
Inferior Occipital Left	Inferior Occipital Right	34,94	0,03
Inferior Frontal Opercular Left	Inferior Frontal Triangular Left	27,75	0,03
ParaHippocampal Left	Inferior Temporal Left	26,86	0,02
Inferior Frontal Opercular Left	Fusiform Left	27,09	0,02
Inferior Occipital Right	Inferior Temporal Right	22,10	0,02
Calcarine Right	Middle Temporal Left	22,09	0,01
Inferior Occipital Right	Middle Temporal Right	21,13	0,01
Middle Frontal Orbital Right	Inferior Temporal Left	20,44	0,00
Middle Temporal Left	Middle Temporal Right	26,96	-0,04
Cuneus Right	Postcentral Right	20,69	-0,04
Postcentral Left	Postcentral Right	20,39	-0,06
Calcarine Right	Postcentral Right	24,32	-0,07
Precentral Right	Anterior Cingulate Right	21,79	-0,09
Middle Frontal Orbital Right	Postcentral Left	20,33	-0,11
Inferior Frontal Triangular Right	Middle Frontal Orbital Right	24,78	-0,11
Anterior Cingulate Right	Postcentral Left	24,86	-0,12
Superior Occipital Left	Postcentral Right	20,23	-0,12
Middle Frontal Right	Anterior Cingulate Right	21,17	-0,12
Superior Frontal Orbital Right	Middle Frontal Orbital Right	22,38	-0,13
Lingual Right	Postcentral Right	22,57	-0,13
Superior Frontal Orbital Right	Postcentral Left	26,22	-0,13

Fusiform Right	Postcentral Right	20,56	-0,15
Postcentral Right	Superior Temporal Pole Right	20,34	-0,17
Precentral Right	Superior Frontal Orbital Left	20,61	-0,17
Middle Frontal Right	Middle Frontal Orbital Right	24,93	-0,17
Anterior Cingulate Right	Inferior Occipital Left	21,62	-0,18
Rectus Left	Postcentral Right	27,42	-0,22
Superior Occipital Left	Superior Occipital Right	20,41	-0,22
Superior Frontal Orbital Right	Postcentral Right	34,14	-0,23
Insula Right	Anterior Cingulate Right	24,36	-0,23
Inferior Frontal Triangular Right	Anterior Cingulate Right	28,32	-0,24
Precentral Right	Superior Frontal Orbital Right	26,45	-0,24
Anterior Cingulate Right	SupraMarginal Right	25,07	-0,27
Middle Frontal Orbital Right	Insula Right	22,37	-0,27
Precentral Right	Rectus Left	24,36	-0,28
Anterior Cingulate Right	Superior Temporal Right	23,77	-0,29
Middle Frontal Orbital Right	Insula Left	23,12	-0,30
Precentral Right	Rectus Right	21,99	-0,34
Rolandic Operculum Left	Anterior Cingulate Right	23,85	-0,36
ParaHippocampal Right	Postcentral Right	25,27	-0,37
Rectus Right	Insula Right	20,66	-0,37
SupraMarginal Right	Paracentral Lobule Right	20,16	-0,37
Precentral Left	Hippocampus Right	27,17	-0,40
Precentral Left	Rectus Right	24,79	-0,41
Superior Frontal Orbital Right	Insula Left	25,00	-0,42
Anterior Cingulate Right	Fusiform Right	24,85	-0,44
Inferior Frontal Orbital Right	Middle Frontal Orbital Right	29,45	-0,48
Precentral Left	Superior Temporal Pole Right	21,07	-0,50
Inferior Frontal Opercular Right	Rectus Left	29,48	-0,53

Superior Frontal Orbital Right	Cuneus Left	26,91	-0,57
Superior Frontal Right	Anterior Cingulate Right	24,02	-0,59
Insula Left	Superior Temporal Pole Right	23,97	-0,60
Rectus Right	Cuneus Right	20,53	-0,63
Anterior Cingulate Right	Fusiform Left	32,38	-0,65
Anterior Cingulate Right	ParaHippocampal Right	26,45	-0,67
Insula Left	Precuneus Right	21,08	-0,69
Superior Frontal Orbital Right	Superior Occipital Left	25,15	-0,69
Precentral Right	Insula Left	22,06	-0,69
Superior Frontal Left	Superior Temporal Pole Right	24,43	-0,78
Insula Left	Postcentral Right	23,25	-0,83
Superior Frontal Left	Hippocampus Right	27,68	-1,16
Supplementary Motor Area Left	Rectus Right	20,23	-1,71

Table S6. Selected models based on acESI feature estimated by NN-SLASSO method.

acESI			
Name ROI 1	Name ROI 2	Replicability	Beta in Best Model
Middle Cingulate Right	Precuneus Left	22,47	19,69
Posterior Cingulate Right	Precuneus Left	24,31	6,08
Insula Left	Cuneus Left	24,43	1,42
Posterior Cingulate Left	Paracentral Lobule Left	22,34	1,33
Middle Cingulate Right	Inferior Temporal Left	24,11	1,28
Middle Cingulate Right	Inferior Occipital Right	22,41	0,87
Posterior Cingulate Left	Inferior Temporal Left	23,23	0,82
Rolandic Operculum Left	Middle Temporal Pole Right	21,39	0,80
Posterior Cingulate Left	Fusiform Left	19,88	0,67
Inferior Frontal Orbital Left	Lingual Left	19,60	0,32
Inferior Frontal Orbital Right	Inferior Temporal Left	23,33	0,30
Rolandic Operculum Left	Middle Temporal Right	22,62	0,29
Inferior Frontal Triangular Right	Middle Temporal Pole Left	22,07	0,29
Inferior Frontal Triangular Left	Fusiform Right	47,21	0,28
Anterior Cingulate Left	Inferior Temporal Left	19,71	0,27
Insula Right	Fusiform Left	27,65	0,26
Inferior Frontal Opercular Left	Middle Temporal Left	33,62	0,25

Inferior Frontal Orbital Left	Inferior Temporal Right	39,07	0,21
Middle Frontal Orbital Left	Inferior Temporal Left	28,41	0,20
Middle Frontal Orbital Left	Inferior Temporal Right	24,48	0,19
Rectus Left	Middle Temporal Right	22,81	0,19
Middle Frontal Left	Middle Temporal Right	34,92	0,18
Inferior Frontal Opercular Left	Inferior Temporal Left	29,04	0,18
Inferior Temporal Left	Inferior Temporal Right	48,20	0,17
Middle Temporal Right	Inferior Temporal Left	40,71	0,17
Inferior Occipital Left	Superior Temporal Right	25,93	0,17
Middle Frontal Left	Superior Temporal Right	27,07	0,16
Inferior Frontal Opercular Left	Middle Temporal Right	25,80	0,15
Middle Temporal Pole Left	Inferior Temporal Right	28,49	0,15
Middle Frontal Left	Inferior Temporal Left	26,09	0,14
Superior Frontal Orbital Left	Inferior Temporal Right	19,94	0,14
Inferior Frontal Triangular Right	Inferior Temporal Left	35,92	0,13
Lingual Left	Inferior Temporal Right	34,08	0,13
Superior Temporal Right	Inferior Temporal Right	27,51	0,12
Inferior Frontal Triangular Left	Middle Temporal Right	43,02	0,12
Lingual Left	Middle Temporal Right	37,03	0,12
Inferior Frontal Triangular Left	Inferior Temporal Right	41,85	0,12
Lingual Left	Inferior Temporal Left	24,64	0,12
Inferior Frontal Triangular Left	Lingual Right	21,93	0,11
Inferior Occipital Left	Inferior Temporal Right	42,69	0,11
Inferior Frontal Orbital Left	Middle Temporal Right	30,73	0,11
Inferior Occipital Right	Inferior Parietal Right	23,21	0,11
Inferior Frontal Opercular Left	Inferior Temporal Right	24,32	0,11
Anterior Cingulate Left	Middle Temporal Right	20,11	0,10

Inferior Frontal Triangular Left	Superior Temporal Right	24,86	0,10
Middle Occipital Right	Inferior Occipital Right	24,57	0,10
Inferior Frontal Triangular Left	Lingual Left	27,00	0,10
Inferior Frontal Triangular Left	Middle Temporal Left	29,23	0,10
Middle Frontal Right	Inferior Temporal Right	31,01	0,10
Middle Frontal Orbital Left	Middle Temporal Right	21,49	0,09
Calcarine Right	Inferior Temporal Left	26,15	0,09
Middle Frontal Orbital Left	Inferior Occipital Left	22,79	0,09
Superior Temporal Left	Inferior Temporal Right	24,57	0,09
Inferior Occipital Right	Middle Temporal Left	26,72	0,09
Inferior Frontal Triangular Left	Fusiform Left	25,93	0,09
Middle Occipital Left	Inferior Temporal Left	32,84	0,09
Inferior Frontal Opercular Left	Calcarine Right	22,73	0,09
Middle Frontal Left	Inferior Temporal Right	20,62	0,08
Middle Occipital Left	Inferior Occipital Right	31,86	0,08
Fusiform Right	Middle Temporal Left	21,61	0,08
Inferior Frontal Triangular Left	Inferior Occipital Right	45,78	0,08
Middle Temporal Left	Inferior Temporal Right	32,58	0,08
Superior Temporal Right	Inferior Temporal Left	24,79	0,08
Inferior Frontal Opercular Left	Fusiform Left	23,84	0,08
Calcarine Left	Inferior Temporal Right	24,79	0,08
Middle Temporal Left	Inferior Temporal Left	24,49	0,07
Inferior Occipital Left	Middle Temporal Right	40,46	0,07
Inferior Frontal Orbital Left	Inferior Occipital Right	23,12	0,07
Inferior Temporal Left	Inferior Temporal Left	46,91	0,06
Fusiform Left	Inferior Temporal Left	28,07	0,06
Inferior Occipital Left	Inferior Temporal Left	38,26	0,06
Calcarine Left	Inferior Temporal Left	21,97	0,05
Middle Occipital Left	Inferior Temporal Right	23,80	0,05
Middle Occipital Right	Middle Temporal Left	27,81	0,05
Calcarine Right	Inferior Occipital Right	20,61	0,05

Fusiform Right	Inferior Temporal Left	23,67	0,05
Fusiform Right	Inferior Temporal Right	24,22	0,05
Middle Occipital Left	Middle Temporal Left	20,88	0,05
Inferior Frontal Triangular Left	Inferior Temporal Left	32,34	0,05
Middle Temporal Right	Inferior Temporal Right	31,36	0,04
Middle Occipital Left	Middle Temporal Right	19,37	0,04
Inferior Frontal Opercular Left	Inferior Occipital Right	29,38	0,04
Inferior Frontal Triangular Right	Inferior Temporal Right	21,29	0,04
Lingual Left	Inferior Occipital Left	22,19	0,03
Inferior Occipital Right	Superior Temporal Right	20,49	0,03
Inferior Occipital Right	Inferior Temporal Left	35,95	0,03
Inferior Occipital Left	Inferior Occipital Right	35,17	0,03
Inferior Occipital Right	Inferior Temporal Right	20,51	0,02
Fusiform Left	Fusiform Left	24,71	0,02
Inferior Temporal Right	Inferior Temporal Right	26,44	0,01
Calcarine Right	Middle Temporal Left	19,05	0,01
Inferior Occipital Right	Inferior Occipital Right	21,13	0,01
Middle Occipital Right	Middle Temporal Right	20,23	-0,01
Middle Frontal Right	Middle Frontal Orbital Right	19,94	-0,01
Middle Temporal Right	Middle Temporal Right	23,86	-0,01
Superior Frontal Orbital Right	Superior Frontal Orbital Right	19,21	-0,01
ParaHippocampal Left	Inferior Temporal Left	22,95	-0,03
Fusiform Right	Middle Temporal Right	19,06	-0,03
Inferior Occipital Right	Middle Temporal Right	22,92	-0,03
Superior Frontal Orbital Right	Anterior Cingulate Right	21,45	-0,04
Middle Frontal Right	Inferior Frontal Orbital Right	20,52	-0,05
Precentral Right	Anterior Cingulate Right	20,76	-0,06
Postcentral Left	Postcentral Right	19,09	-0,07
Anterior Cingulate Right	Postcentral Left	24,85	-0,08
Superior Frontal Orbital Right	Rolandic Operculum Left	21,70	-0,08
Middle Temporal Left	Middle Temporal Right	21,70	-0,09

Superior Frontal Orbital Right	Middle Frontal Orbital Right	24,86	-0,10
Middle Frontal Right	Anterior Cingulate Right	19,35	-0,10
Calcarine Right	Postcentral Right	23,91	-0,11
Inferior Frontal Triangular Right	Middle Frontal Orbital Right	26,04	-0,12
Superior Frontal Orbital Right	Postcentral Left	23,44	-0,13
Precentral Right	Superior Frontal Orbital Right	29,34	-0,17
Lingual Right	Postcentral Right	21,39	-0,18
Middle Frontal Right	Middle Frontal Orbital Right	24,49	-0,19
Superior Frontal Orbital Left	Postcentral Left	21,27	-0,22
Insula Right	Anterior Cingulate Right	22,29	-0,23
Superior Frontal Orbital Right	Postcentral Right	30,97	-0,23
Postcentral Right	Superior Temporal Pole Right	19,61	-0,25
Rectus Left	Postcentral Right	24,02	-0,26
Middle Frontal Orbital Right	Insula Right	25,00	-0,26
Anterior Cingulate Right	SupraMarginal Right	20,49	-0,28
Inferior Frontal Triangular Right	Anterior Cingulate Right	26,39	-0,28
Precentral Right	Middle Temporal Pole Left	21,30	-0,29
Rolandic Operculum Left	Anterior Cingulate Right	23,86	-0,29
Superior Frontal Left	Hippocampus Left	20,34	-0,30
Precentral Right	Rectus Left	20,89	-0,30
Rectus Left	Postcentral Left	19,37	-0,35
Precentral Right	Rectus Right	20,61	-0,37
Superior Frontal Orbital Right	Insula Left	25,59	-0,43
SupraMarginal Right	Paracentral Lobule Right	19,23	-0,44
Anterior Cingulate Right	Superior Temporal Left	21,63	-0,46
ParaHippocampal Right	Postcentral Right	23,71	-0,47
Superior Frontal Right	Anterior Cingulate Right	22,57	-0,47
Inferior Frontal Orbital Right	Middle Frontal Orbital Right	31,18	-0,48
Anterior Cingulate Right	Fusiform Right	20,61	-0,50
Precentral Left	Hippocampus Right	23,01	-0,51

Middle Cingulate Right	Postcentral Left	22,16	-0,57
Precentral Left	Rectus Right	22,16	-0,57
Precentral Right	Insula Left	23,63	-0,60
Inferior Frontal Opercular Right	Rectus Left	28,74	-0,61
Insula Left	Superior Temporal Pole Right	23,63	-0,71
Anterior Cingulate Right	Fusiform Left	30,34	-0,72
Superior Frontal Orbital Right	Cuneus Left	22,51	-0,78
Superior Frontal Orbital Right	Superior Occipital Left	27,35	-0,79
Anterior Cingulate Right	ParaHippocampal Right	22,81	-0,85
Superior Frontal Left	Superior Temporal Pole Right	22,67	-0,91
Insula Left	Postcentral Right	23,36	-1,00
Superior Frontal Left	Hippocampus Right	29,89	-1,08
Supplementary Motor Area Right	Hippocampus Right	19,28	-1,95